Elastic resonant and nonresonant differential scattering of quasifree electrons from $B^{4+}(1s)$ and $B^{3+}(1s^2)$ ions

E. P. Benis,[1,*] T. J. M. Zouros,[2,3,†] T. W. Gorczyca,[4] A. D. González,[5] and P. Richard[1]
[1]*James R. Macdonald Laboratory, Department of Physics, Kansas State University, Manhattan, Kansas 66506-2604, USA*
[2]*Department of Physics, University of Crete, P.O. Box 2208, 71003 Heraklion, Crete, Greece*
[3]*Institute of Electronic Structure and Laser, P.O. Box 1527, 71110 Heraklion, Crete, Greece*
[4]*Department of Physics, Western Michigan University, Kalamazoo, Michigan 49008, USA*
[5]*Consejo Nacional de Investigaciones Cientificas y Tecnicas, Argentina*
(Received 12 December 2003; published 28 May 2004)

High-resolution doubly differential cross-section measurements and calculations for quasifree electrons elastically scattered through 180° from ground-state He- and H-like boron ions are presented. The measurements, covering the entire (for B^{3+}) and (for B^{4+}) Rydberg series populated by resonant excitation, were performed by zero-degree Auger projectile electron spectroscopy of 3.91 MeV B^{4+} and 3.08–7.48 MeV B^{3+} ions in collisions with H_2 targets. The projectile energy dependence study is used to further investigate other background contributions such as direct electron capture, direct excitation, and nonresonant transfer excitation. *R*-matrix calculations, particularly sensitive at this large scattering angle to electron correlation, exchange, and interference effects, are found to be in excellent overall agreement within the electron scattering model.

DOI: 10.1103/PhysRevA.69.052718 PACS number(s): 34.50.Fa, 32.80.Hd, 32.80.Dz

I. INTRODUCTION

Electron-ion *differential* scattering measurements probe the delicate interplay between the electron, the short-range scattering potential due to the electronic structure of the ion, and the long-range Coulomb potential due to the ion's charge [1]. Small-angle ($\theta \lesssim 80°$) electron scattering [2,3] corresponds to distant collisions. Therefore, it is dominated by the ionic Coulomb potential and it exhibits Rutherford scattering behavior, which is well understood [1]. Large-angle ($\theta \gtrsim 80°$) scattering [4] corresponds to a deeper probing of the atomic structure near the distance of closest approach. It is therefore much more sensitive to correlation, exchange [1–4], bound-state resonances, and interference effects [1,5,6], especially at the largest scattering angles around $\theta = 180°$ [3,5]. These effects are particularly enhanced in electron-*ion* collisions since there are many more bound channels available compared to those in electron-*atom* scattering [1].

Electron scattering from highly charged ions (HCI) with just a few electrons, such as H-like and He-like ions, offers some of the simplest testing grounds of atomic structure and collision theory. The formation of bound, doubly excited two- and three-electron states is populated by resonant excitation (RE), an inverse Auger process in which the ionic electron undergoes a Δn excitation in the principal quantum number n while the impinging electron is simultaneously captured. These resonances can then relax either by photon or electron emission, in which case the process is known as dielectronic recombination (DR) or resonant elastic scattering (RES), respectively. *Total* cross sections have been determined for DR [$\Delta n = 0$ from metastable $O^{6+}(1s2s\ ^{3,1}S)$ [7], $\Delta n = 1$ from $O^{7+}(1s)$ [8], and ground-state $C^{4+}(1s^2)$ [9]], as well as from other HCI [10], primarily in ion storage rings with very high precision, by extracting the final charge-changed ions. Even though excellent overall agreement with theory has mostly been found, some information is lost since total cross sections do not include interference effects between cross terms (see Sec. IV B below), which can only be fully investigated by *differential* electron-ion scattering measurements.

II. DIFFERENTIAL ELECTRON SCATTERING FROM HCI

Differential electron-ion scattering measurements are still very scarce. The extremely low luminosity inherent in these types of crossed or merged beam experiments limits the detection count rates, requiring special low signal-to-noise techniques and ultrahigh-vacuum (UHV) conditions of better than $\sim 10^{-10}$ Torr. Some of the first pioneering experiments were performed at the Jet Propulsion Laboratory in the beginning of the 1980s using electron-energy-loss spectroscopy with a merged-beam apparatus to study differential impact excitation of Mg^+, Zn^+, and Cd^+ ions in the small-angle scattering range $\theta = 4° - 16°$ [11–13]. More recently, Huber *et al.* [14], using a double-stage cylindrical energy spectrometer, reported on the measurement of $3s \rightarrow 3p$ excitation differential cross sections in the angular range between 13° and 29° for 100 eV electron impact on Ar^{7+} ions. These studies were extended to also include elastic scattering of heavy multicharged ions (Xe^{6+}, Xe^{8+}, and Ba^{2+}) by electrons of collision energy below 50 eV in the angular range between 30° and 90° [2]. The same group also reported on larger angle elastic nonresonant scattering measurements (between 32° and 148°) for both Xe^{3-6+} and Ar^{8+} ions [4]. A crossed *E* and *B* field trochoidal analyzer was used by Guo *et al.* to investigate the backscattering of electron impact excitation of

*Present address: Institute of Electronic Structure and Laser, P.O. Box 1527, 71110 Heraklion, Crete, Greece.
†Email address: tzouros@physics.uoc.edu

$Ar^{7+}(3s \rightarrow 3p)$ [15]. A similar technique was used by Greenwood *et al.* [3] to extend the angular range all the way from 120° to 170° for 3.3 eV electron scattering of Ar^+ ions, thus including a good part of the very sensitive large-angle scattering region [16]. Finally, Srigengan *et al.* in 1996 [17] studied elastic electron scattering from Na^+ ions over the angular range $\theta = 25° - 95°$. To our knowledge, there have been no new results reported since then. Furthermore, *no* resonances have ever been traced out in any type of merged or crossed beam electron-ion *scattering* experiments. A recent review of the field has been given by Williams [1].

Quasifree electron-ion differential scattering measurements overcome the low luminosity problem by exploiting the $\sim 10^8$ times higher luminosity of collisions between *lightly bound* target electrons and energetic HCI produced from an accelerator. The luminosity increase primarily results from the much higher densities possible with neutral gas targets. The lightly bound (quasifree) target electrons, under the right conditions, scatter from the ion as if they are free. Over the past 20 years, investigations covering a large variety of projectile ions in energetic collisions with mostly H_2 and/or He targets showed that the excitation of projectile ions contains substantial contributions from direct projectile-electron-target-electron (e-e) interactions over and above the usual projectile-electron-target-nucleus (e-n) interactions. The collisional energy dependence of the measured projectile excitation cross sections exhibited characteristics usually associated with electron impact phenomena [18–21]. Thus, strong resonance phenomena observed in resonance transfer excitation (RTE) measurements [22,23] could be associated with RE, radiative electron capture (REC) corresponded to radiative recombination (RR) [24–27] and electron impact threshold, target recoil and electron exchange effects, usual signatures of electron impact excitation and ionization, were clearly identified in the excitation [28–30] and ionization [31–37] of projectile ions in ion-atom collisions, respectively.

In particular, when the projectile velocity V_p is much larger than the velocity v of the bound scattering electron, i.e., when $\nu \equiv V_p/v \gg 1$, the so-called impulse approximation (IA) [6,21,36,38–40] is valid, describing the quasifree electron-ion interaction as the interaction of a *free* electron with a momentum p_z distribution given by its Compton profile $J(p_z)$. More recently, it has become evident that processes describing electrons emitted from ion-atom collisions, such as, for example, the binary encounter electrons (BEe) [40,41] and RTEA [23] electrons (Auger electrons ejected from doubly excited ionic states produced by RTE), where the contributions from target-nucleus interactions can be minimized, basically correspond to the processes of nonresonant elastic (for BEe) and resonant (for RTEA) electron-ion scattering. A unified treatment of both resonant and nonresonant electron-ion scattering in ion-atom collisions thus seemed appropriate and became known as the electron scattering model (ESM) [6,41,42]. The ESM incorporates the IA in the first half of the scattering process and includes both resonant and nonresonant scattering in one coherent approach [6].

Before the ESM, the BEe and RTEA processes were always treated separately. These processes have been extensively studied in the literature and numerous articles can be found both for BEe (see, for example, [40,43–49]) and RTEA (see, for example, [23,38,50–56]). The realization that both RTEA and BEe could be treated within the ESM on the same footing as quasifree elastic resonant (for RTEA) and nonresonant (for BEe) electron scattering from HCI led to the use of the powerful electron scattering R-matrix technique to describe both processes. An evolution in nomenclature reflecting this deeper understanding [41,42,49,57–60] has followed, and thus the term RES, which includes not only the resonant part but also interferences between the resonant and nonresonant part, is used here instead of the older RTEA, while the intermediate resonant state population mechanism will be referred to as RE. RTEA singly differential cross sections (SDCS) measured prior to 1996 have always been found to be smaller than the existing theory, while RTEX (RTE measurements of the emitted x-ray [22] rather than Auger electrons) SDCS have always been in good agreement with theory [23]. In RTEX (just like DR), it is well known that the direct contribution due to RR is usually negligible near resonance, as is the interference term. On the other hand, in RTEA (just like electron scattering), the direct and interference terms are quite sizable, and the interference often is a reducing factor from a purely Lorentzian feature, as is shown here. Thus, the older RTEA formulations of the past based on simple Lorentzian considerations will generally work for RTEX but not for RTEA.

Quasifree electron-ion scattering investigations have been refined over the past decade [21,41,49,57,61,62], substantially reducing undesirable *nucleus*-ion contributions (e.g., e-n interactions) by choosing favorable collision conditions and low-Z targets [21,46]. Good agreement with more recent R-matrix calculations have caught the attention of the electron-ion scattering community [1,10] and include measurements of resonant and nonresonant elastic [49,58] and inelastic [42,57] electron scattering from H-like ions, as well as superelastic scattering from metastable He-like ions [59,60]. Recent reviews of quasifree electron scattering can be found in Refs. [21,41,57,62,63].

The unified BEe-RTEA treatment first proposed by Bhalla [6], as also early ESM-R-matrix investigations [64], were focused primarily on the $2p^2\ ^1D$ state, the *single* strong RE line seen in the $2lnl'$ Rydberg series of H-like ions [58]. Good agreement between theory and experiment was found. This comparison, however, only tests calculations over the very narrow energy range of a single line (e.g., the $2p^2\ ^1D$). Opening up the much richer resonance structure of the $1s2lnl'$ Rydberg series [9] by scattering from *ground-state* He-like ions allows for a much more extensive testing of theory. However, such absolute *differential scattering* measurements have *never* been performed, primarily because He-like ions usually include a large fraction of $1s2s\ ^3S$ metastable states $f_{^3S}$ [56,65], which is hard to measure directly. Recently, we reported on a new technique for obtaining almost metastable-free $B^{3+}(1s^2)$ beams [65,66]. Here, we utilize this technique to measure the absolute doubly differential cross section (DDCS) of 180° elastic (resonant and nonresonant) quasifree electron scattering from *ground-state* He-like $B^{3+}(1s^2)$ ions. State-of-the-art R-matrix calculations utilized within the ESM are compared to the data. Prelimi-

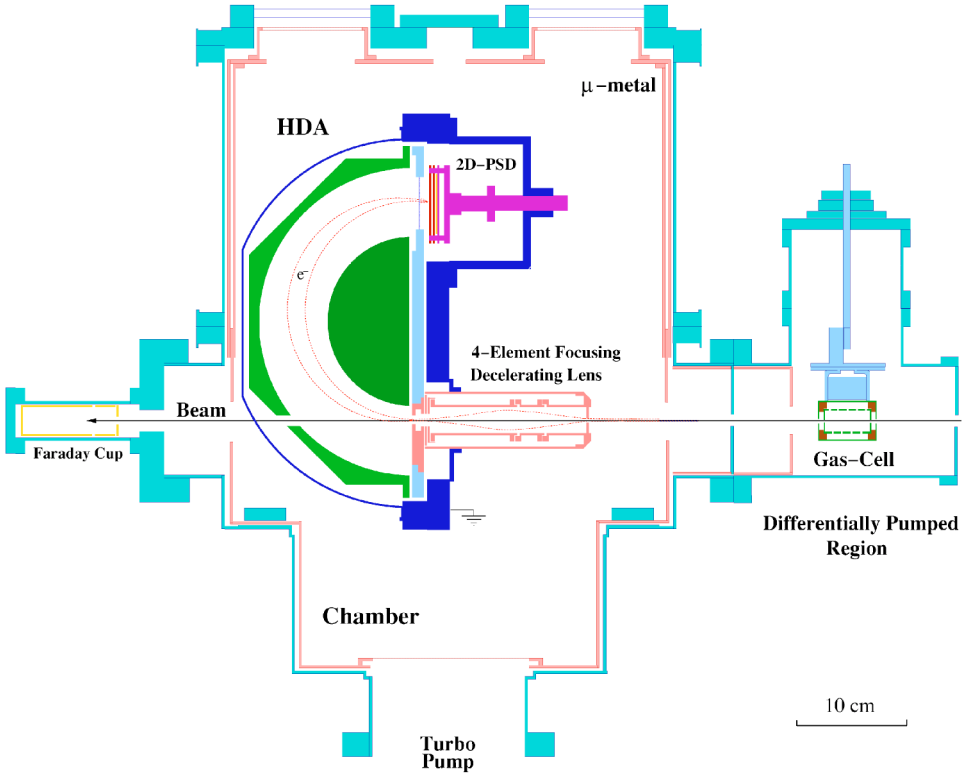

FIG. 1. (Color online) Schematic of the zero-degree Auger projectile electron spectroscopy setup at the JRML. The ion beam interacts with the gas target, confined by the gas-cell, transverses the spectrograph, and exits through a hole at the back. The ion beam current is recorded at the Faraday Cup for normalization purposes. The electrons emitted from the target area are focused and decelerated by the four-element lens into the hemispherical deflector analyzer (HDA) entry. After a deflection through 180°, they are detected at the two-dimensional position sensitive detector (2D-PSD).

nary results were presented at conferences [63] and more recently published as a Rapid Communication [67]. A more extensive coverage is also given here of both theoretical and experimental details including results and analysis of collisional energy dependence of RES DDCS. In Secs. III and IV, a more detailed account of both experimental and theoretical procedures is presented. In Secs. V and VI, the data are presented, analyzed, and discussed, with a summary and conclusion following in Sec. VII.

III. EXPERIMENT

The measurements were performed in the J. R. Macdonald Laboratory (JRML) at Kansas State University utilizing the 7 MV EN tandem Van de Graaff accelerator. The B^{3+} ions were produced directly from the tandem accelerator after colliding the negatively charged incident B^- beam with the accelerator's N_2 gas stripper. In this way, less than ~3% of the metastable $1s2s\ ^3S$ state was produced [69]. Such a practically pure ground-state $B^{3+}(1s^2)$ beam was essential for the experiments, as the strong presence of metastable ions would not only complicate the spectra both in line identification and mechanisms involved [67], but also introduce uncertainties in the absolute DDCS determination associated with the necessary determination of the metastable fraction [65,69,70]. The B^{4+} beams were obtained after post-stripping the primary B^{3+} beams in thin (5 $\mu g/cm^2$) carbon foils prior to their magnetic selection. The F^{8+} ion beams, used for benchmark measurements, were produced by post-stripping the F^{4+} primary beams. All ion beams were collimated down to 1.5 mm^2 by two pairs of slits, and finally collided with the H_2 target in a 5-cm-long gas-cell.

A single-stage biased paracentric [71–73] hemispherical spectrograph, incorporating a hemispherical deflector analyzer (HDA), a 40 mm active diameter two-dimensional position sensitive detector (PSD) with resistive anode encoder and a 4-element focusing lens was utilized to record the electron yields at zero degrees with respect to the ion-beam direction, $\theta_L = 0°$. The operation and performance of the novel biased paracentric spectrograph have been partially described in the literature [74–76]. In short, as shown in Fig. 1, the electrons emitted from the gas-cell at $\theta_L = 0°$ within a solid angle of 0.848° subtended by the 4-mm-diam entrance lens aperture were focused into the analyzer, where they were energy analyzed and detected at the PSD. The large (6-mm -diam) size of the HDA entry assured a 100% electron transmission over the deceleration range used. The double focusing properties of the HDA combined with the use of the PSD allowed for a very high detection efficiency, since the spectrum was recorded simultaneously over an energy window of about ~20% of the nominal pass energy. The measurements were performed in high-resolution mode using a deceleration factor $F = 4$, corresponding to a full width at half maximum (FWHM) energy resolution of ~0.15% in the laboratory frame (or ~0.30% in the projectile rest frame). In some cases, the spectra were obtained after matching four or five overlapping energy windows. An example is shown in Fig. 2, where the zero-degree DDCS electron spectra for the 4.00 MeV $B^{3+}(1s^2)+H_2$ collision system are plotted in the laboratory frame.

All measurements were taken under single-collision conditions using an H_2 gas target at a pressure of 20 mTorr. The gas-cell was differentially pumped, establishing a chamber pressure of 3.5 μTorr at a gas-cell pressure of 20 mTorr, while the gas-cell's differentially pumped region maintained

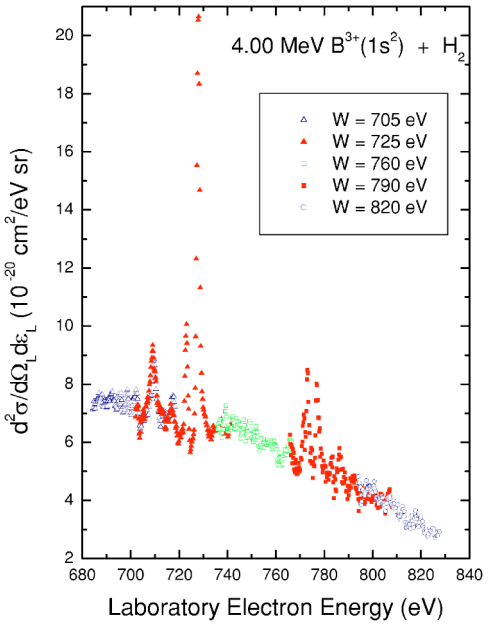

FIG. 2. (Color online) Zero-degree laboratory (L) electron spectra obtained in 4.00 MeV $B^{3+}(1s^2)+H_2$ collisions. The data were recorded after overlapping five different spectra segments of progressively larger tuning energies W. A deceleration factor of $F=4$ was used for all spectra.

a pressure of 30 μTorr. However, this differential pumping was inadequate and contributions from outside the gas-cell accounted for up to 80% of the signal. Thus, a second background spectrum was also taken by flooding the beam line with H_2 (empty gas-cell) from an independent orifice to the same chamber pressure as in the loaded gas-cell measurement. This spectrum was then subtracted from the loaded gas-cell spectrum, resulting in a background-free electron spectrum. MKS Baratron capacitance manometers were used with an electronic valve feedback system to maintain a constant pressure throughout the measurements.

The ion beam was collected in a shielded Faraday cup (FC) with electron suppression located after the exit aperture of the spectrograph. The recorded beam current was used for the data acquisition charge normalization. Typical beam currents were of the order of a few nA, while in some cases (e.g., B^{4+}) currents as low as 100 pA could be utilized, thus demonstrating the much improved efficiency of the new spectrograph [74,75] over the older two-stage tandem electron slit spectrometer [77]. Thus, traditionally low intensity boron ion beams not previously practical could now be used in our measurements. Some of the important experimental parameters are listed in Table I.

IV. DDCS CALCULATIONS

A. Electron scattering model

The ESM is important, as it provides a simple and general framework for linking electron scattering processes in the two rather distinct fields of ion-atom and ion-electron collisions [21]. As already mentioned, at the heart of the ESM is the IA, which is known to be valid when $\nu \gg 1$. Thus, during the collision time, the target electron may be considered to be fixed. Viewing the collision process from the projectile rest frame, the electron can be treated as a free particle approaching the projectile ion with a velocity $\vec{V}=\vec{V}_p+\vec{v}$. Then, the electron impact energy in the projectile frame ε is written as (in atomic units) [21]

$$\varepsilon = \frac{1}{2}(\vec{V}_p + \vec{v})^2 = \frac{1}{2}V_p^2 + p_z V_p + \frac{1}{2}\sum_j p_j^2, \qquad (1)$$

where p_j is the momentum components in the $j=x,y,z$ directions. Brandt, in the first IA model applied to ion-atom collisions [38], neglected the p_j^2 terms. Itoh *et al.* [78] advanced Brandt's approximation by subtracting also the ionization energy of the active target electron E_I, as a further correction. Lee *et al.* [40] improved the agreement between

TABLE I. Table of experimental parameters [68].

	Value	Description
R_1	72.4 mm	HDA inner radius
R_2	130.8 mm	HDA outer radius
R_0	82.6 mm	Center of HDA entry aperture
d_{PSD}	40 mm	Active diameter of PSD
d_{LE}	4 mm	Diameter of lens entry aperture
d_0	6 mm	Diameter of HDA entry aperture
$\Delta\theta$	0.868°	Full angular acceptance
t_{DTC}	1–1.2	Measured dead time correction
N_I	$(3-6)\times 10^{12}$	Number of ions collected
L_c	51.75 mm	Effective length of target gas-cell
n	6.44×10^{14} molecules/cm^3	density of H_2 at 20 mTorr and 300 K
l	264 mm	Mean target to lens distance
$\Delta\Omega$	1.8×10^{-4} sr	Full acceptance solid angle
T	0.81	Overall grid transmission
η	~0.20	Absolute efficiency of PSD

the IA model and experiment by keeping the E_I correction along with the p_z^2 term while ignoring the p_x^2 and p_y^2 terms. Following Lee's approximation, Eq. (1) can be written as

$$\varepsilon \simeq \frac{1}{2}V_p^2 + p_z V_p + \frac{1}{2}p_z^2 - E_I. \tag{2}$$

Thus, within the IA, the electron DDCS in the projectile rest frame for the ion-atom collision can be related to the SDCS, $d\sigma(\varepsilon,\theta)/d\Omega$, for the free electron-ion collision as

$$\left.\frac{d^2\sigma(\varepsilon,\theta)}{d\Omega d\varepsilon}\right|_{\text{quasifree}} = \left.\frac{d\sigma(\varepsilon,\theta)}{d\Omega}\right|_{\text{free}} \frac{J(p_z)}{V_p + p_z}, \tag{3}$$

where

$$p_z = \sqrt{2(\varepsilon + E_I)} - V_p, \tag{4}$$

obtained by solving Eq. (2) for p_z, and

$$J(p_z) = \int\int dp_x dp_y |\psi(\vec{p})|^2 \tag{5}$$

is the Compton profile which gives the probability to find a specific target electron with a z-momentum component p_z, where z is the direction of the projectile velocity. $\psi(\vec{p})$ is the impinging target electron wave function in momentum space. Calculated Hartree-Fock Compton profiles are available in the literature [79], while for H_2 and He targets, analytic expressions have been derived from experimental data [80].

In a typical DDCS calculation, first the SDCS for the free electron is calculated as a function of the electron energy ε. Then p_z is calculated for each ε at the particular ion velocity V_p and target species binding energy according to Eq. (4). Finally, the Compton profile $J(p_z)$ is evaluated at p_z and the DDCS for the quasifree electron is obtain as given by Eq. (3). In this procedure, the free-electron SDCS need only be calculated once at each ε and can then be used for any ion collision energy required. We have used this procedure to evaluate DDCS in our ion-atom collisional energy dependence study below with the free-electron SDCS evaluated by the R-matrix method.

B. Theoretical electron-ion scattering cross sections

1. SDCS

All existing RTEA calculations to date have applied the IA formulation presented in Eq. (3). The differences between calculations have to do primarily with the formula used for the free-electron SDCS, i.e., $d\sigma/d\Omega|_{\text{free}}$ and its evaluation. Here we use the SDCS formula given by Griffin and Pindzola [5]. For scattering from an initial ionic $L_i=0$ state to a final ionic $L_f=0$ state, the initial and final angular momenta for a given partial wave are equal ($l_i=l_f\equiv l$). Then the angular differential cross-section expression [Eq. (4) in Ref. [5]] can be considerably simplified, and is given in atomic units per steradian (a.u./sr) by

$$\frac{d\sigma_{if}}{d\Omega} = \frac{d\sigma_{if}^{\text{Coul}}}{d\Omega} + \frac{d\sigma_{if}^{\text{int}}}{d\Omega} + \frac{d\sigma_{if}^{\text{sr}}}{d\Omega} \tag{6}$$

with

$$\frac{d\sigma_{if}^{\text{Coul}}}{d\Omega} = \delta_{if}\frac{(q/k_i)^2}{4k_i^2\sin^4(\theta/2)} \quad \text{(Rutherford term)}, \tag{7}$$

$$\frac{d\sigma_{if}^{\text{int}}}{d\Omega} = -\,\delta_{if}\frac{(q/k_i)}{4(2S_i+1)k_i^2\sin^2(\theta/2)} \quad \text{(interference term)}$$
$$\times \text{Im}\left[e^{-i(q/k_i)\ln[\sin^2(\theta/2)]}\sum_S (2S+1)\sum_{l=0}^{l_{\max}}(2l+1)P_l(\cos\theta)e^{2i[\sigma_l(q/k_i)-\sigma_0(q/k_i)]}T_{Sll}(i\to f)\right], \tag{8}$$

$$\frac{d\sigma_{if}^{\text{sr}}}{d\Omega} = \frac{1}{8(2S_i+1)k_i^2}\sum_S (2S+1)\sum_{l,l'=0}^{l_{\max}}(2l+1)(2l'+1)\sum_{\lambda=|l-l'|}^{l+l'}(2\lambda+1)\begin{pmatrix} l & l' & \lambda \\ 0 & 0 & 0\end{pmatrix}^2 P_\lambda(\cos\theta)$$
$$\times\, e^{i[\sigma_l(q/k_i)+\sigma_l(q/k_f)-\sigma_{l'}(q/k_i)-\sigma_{l'}(q/k_f)]}T^*_{Sl'l'}(i\to f)T_{Sll}(i\to f) \quad \text{(short-range term)}, \tag{9}$$

where

$$\sigma_l(x) = \arg[\Gamma(l+1-ix)] \tag{10}$$

is the Coulomb phase shift. Here, $\varepsilon=\frac{1}{2}k_i^2$ and $\varepsilon_f=\frac{1}{2}k_f^2$ are the initial and final energies of the electron, respectively, and l and l' are the orbital angular momenta of the electron. For B^{4+}, the sum over total spins is from $S=0$ to $S=1$. For B^{3+}, the sum includes only $S=\frac{1}{2}$, if either the initial target ionic spin $S_i=0$ or the final target ionic spin $S_f=0$; for triplet-triplet scattering, then the sum is from $S=\frac{1}{2}$ to $S=\frac{3}{2}$. For $\theta=180°$, $P_\lambda(\cos\theta)=(-1)^\lambda$. The sums over l and l' extend from 0 to the maximum partial wave included, $l_{\max}$. $T^{LS\Pi}_{l_i l_f}$ is an element of the transition matrix for a given total angular momentum L, total spin S, and parity Π connecting initial state i to final state f [5]. For the particular case at hand, $L_i=L_f=0$, it follows that $l_i=l_f=l=L$, with $\Pi=(-1)^l$ so that we can use the

shorthand notation $T_{Sll}(i \to f) \equiv T_{ll}^{lS(-1)^l}$. Thus, all the effort goes into the calculation of the T matrices, which are then inserted into Eqs. (8) and (9) to evaluate the differential cross sections. The T matrices, in this $L_i = L_f = 0$ case, are diagonal in the quantum number $l(l')$ and need to be evaluated on a very dense energy grid so as to resolve sufficiently all resonances. Various approaches have been used in evaluating the transition matrices, such as close-coupling, distorted wave, and/or R-matrix methods. Differences between the various approaches have been observed in the evaluation of the SDCS, particularly at $\theta = 180°$, even though total cross sections give very similar results [5]. Here we use the R-matrix approach described in Sec. IV B 3.

The first term, given by Eq. (7), is the Coulomb term corresponding to the long-range, pure Coulombic potential for an ion with charge state q. Elastic scattering of quasifree electrons from ions gives rise to the BEe peak already mentioned [47]. In particular, when the ion is *bare*, the other two scattering terms are zero since there can be no short-range (direct or resonant) amplitude, and therefore no interference term either. In this case, the well-known Coulomb scattering SDCS formula has been shown to be valid, demonstrating unambiguously the validity of the ESM in collisions with two-electron targets such as H_2 and He [40]. Even in the case of many-electron targets such as Ne, Ar, Xe, and Kr [81], as well as complicated molecules [82], in which electrons from different shells can contribute with different Compton profiles and binding energies, the ESM has also been shown to be a good approximation. Earlier studies of the Coulomb or BEe contributions in collisions with *nonbare* or *clothed* ions have also shown the validity of the ESM [83,84]. The nonresonant part of the DDCS from the sum of all three terms for 180° is known to increase with decreasing q [44], an effect first explained in terms of classical scattering glory effects [85] and consistent with the full quantal R-matrix treatment provided by the above Eqs. (6)–(9).

The third term, given by Eq. (9), corresponds to the short-range potential which includes all atomic structure contributions (resonances, correlation and exchange effects, polarization, etc.) as well as nonresonant contributions. Interferences between these two contributions are also evident (see dotted line in Fig. 3).

Finally, the second term, given by Eq. (8), is due to the interference between the Coulomb and the short-range terms. We note that the interferences present in the second and third terms may add up destructively or constructively depending on the phase.

The first two terms contribute only to elastic scattering $(i = f)$ and are zero for either inelastic scattering [42,57,86] or superelastic scattering [59,60] from ions. The third term contributes to both elastic $(i = f)$ and inelastic $(i \neq f)$ scattering and is the term amenable to investigation in electron-atom scattering studies. Clearly, only electron scattering from ions gives rise to the first two terms, thus providing an important example of the application of the well-known two-amplitude long-range-short-range scattering formalism taught in many graduate text books (see, for example, [87]) in the realm of atomic collisions.

The contributions from the three different terms of Eq. (6) are shown in Fig. 3 for the case of 180° elastic electron scattering from $B^{3+}(1s^2)$ ions.

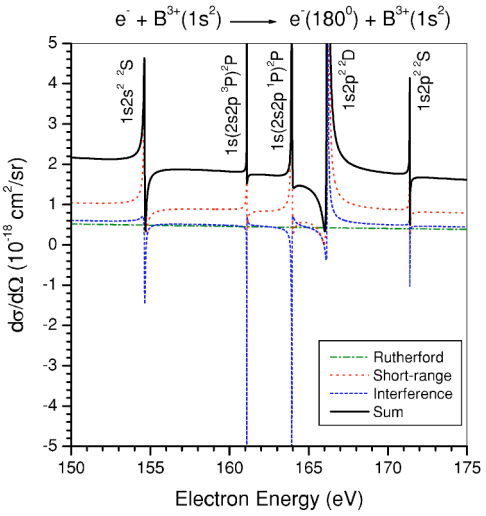

FIG. 3. (Color online) Blow-up of R-matrix calculations showing the contribution of the three individual terms of Eq. (6) for 180° elastic electron scattering from $B^{3+}(1s^2)$. Both interference and short-range terms are seen to have substantial nonresonance contributions.

2. Total cross-section calculations

Total electron scattering cross sections cannot be directly extracted by integrating Eq. (6) over solid angle $d\Omega = d(\cos\theta)d\phi$, since the first two terms would give infinite contributions. However, contributions from the third term are finite and considerable simplifications arise, leading to the expression

$$\sigma_{if}^{\mathrm{sr}} = \int \frac{d\sigma_{if}^{\mathrm{sr}}}{d\Omega} d\Omega = \frac{\pi}{2(2S_i+1)k_i^2} \sum_{l=0,S}^{l_{\max}} (2S+1) \times (2l+1)|T_{Sll}(i \to f)|^2, \tag{11}$$

where we have used the following identities:

$$\int_0^{\pi} P_\lambda(\cos\theta) d\cos\theta = 2\delta_{\lambda 0} \tag{12}$$

and

$$\begin{pmatrix} l & l' & 0 \\ 0 & 0 & 0 \end{pmatrix}^2 = \frac{\delta_{ll'}}{(2l+1)}, \tag{13}$$

The total cross section, $\sigma_{if}^{\mathrm{sr}}$, is seen to have quite a different energy dependence than the 180° differential cross section, demonstrating the large anisotropy involved. This is shown clearly in Fig. 4, where $\sigma_{if}^{\mathrm{sr}}/4\pi$, $d\sigma_{if}/d\Omega$ [the monopole term only, i.e., $l = 0$ in Eq. (8) and $\lambda = 0$ in Eq. (9)], and the full $d\sigma_{if}/d\Omega$ [Eq. (6)] are compared. Since the differential cross-section expression involves *cross terms* between lower and higher partial wave symmetries l, l' [see Eq. (9)], it was necessary to include *more* partial waves than were needed to converge the total cross section $\sigma_{if}^{\mathrm{sr}}$ [which does not involve cross terms—see Eq. (11)].

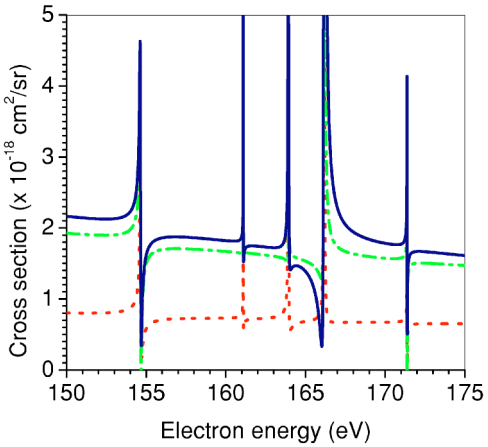

FIG. 4. (Color online) Comparison between different *R*-matrix cross-section calculations for 180° electron scattering from $B^{3+}(1s^2)$. Continuous line: full calculation of $d\sigma_{if}/d\Omega$ [see Eq. (6)]. Dashed-dot line: $d\sigma_{if}/d\Omega$ but only for the monopole contribution, i.e., just the partial wave with $l=0$ in Eq. (8) and just $\lambda=0$ in Eq. (9). The monopole part is seen to contribute a substantial part (but not all) of the cross section. The extra amount is due to the anisotropic, higher-order multipole contributions. Dashed line: short-range total cross section, $\sigma_{if}^{sr}/4\pi$ [see Eq. (11)].

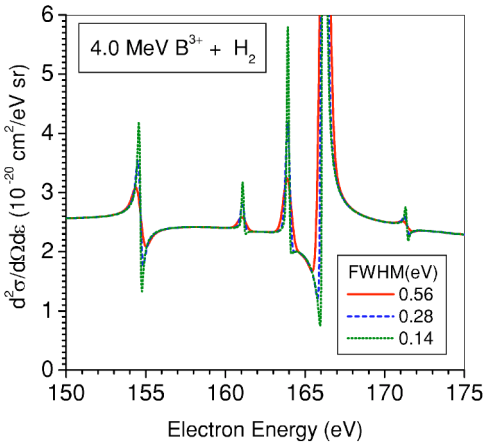

FIG. 5. (Color online) Effect of finite-energy resolution on the interference structures in 4.0 MeV $B^{3+}(1s^2)+H_2$ for the region around the $1s2p^2\ ^1D$ state. Continuous line: Actual experimental resolution used in this work. Discontinuous lines: Other resolutions.

3. R-matrix calculations

The theoretical elastic electron scattering cross section, $d\sigma(\varepsilon,\theta)/d\Omega$, was obtained using an *R*-matrix method [88]. First, for the B^{3+} calculation, a basis set of physical orbitals $nl=\{1s,2s,2p,3s,3p,3d\}$ was determined from $1snl$ configuration-averaged Hartree-Fock calculations [89]. Then all the *N*-electron configurations $nln'l'$ $(n,n'=1,2,3$ and $l,l'=0,1,2)$ were used to describe the 11 lowest states of B^{3+}: $1s^2\ ^1S$, $1s2s\ ^{1,3}S$, $1s2p\ ^{1,3}P$, $1s3s\ ^{1,3}S$, $1s3p\ ^{1,3}P$, and $1s3d\ ^{1,3}D$. A basis of 40 additional orthogonal orbitals was coupled to these 11 configuration-interaction target states to represent the resonance or continuum wave functions of B^{2+}. To compensate for the necessary orthogonality and to include extra correlation, all $(N+1)$-electron configurations $nln'l'n''l''$ were also included here. [For the B^{4+} and F^{8+} calculations, hydrogenic orbitals $nl=\{1s,2s,2p,3s,3p,3d\}$ were used to describe exactly the lowest six states of B^{4+} and F^{8+}, 40 additional orbitals were coupled to these to describe the resonance or continuum wave functions of B^{3+} and F^{7+}, and all $(N+1)$-electron configurations $nln'l'$ were also included.]

With this atomic structure, the *R*-matrix suit of codes was utilized to compute scattering transition matrices $T_{i\to f}(\varepsilon)$. A short description of our *R*-matrix (based on the Belfast suit of inner-region codes [90] and the University College London suit of outer-region codes [91]) ESM approach has already been given for calculations of RES from the $B^{3+}(1s^2)$ ground state [67]. In our calculations, partial waves up to $l_{max}=9$ were required to converge the expressions in Eq. (6) and an energy grid of 10 000 points was used for ε_i.

The Auger transition energies and total widths Γ were accurately determined by a Lorentzian fit of the form $\Gamma/[(\varepsilon-\varepsilon_R)^2+(\Gamma/2)^2]$ to the trace of Smith's time delay matrix [92] $Q=iSdS^{\dagger}/d\varepsilon$, where *S* is the scattering matrix and ε_R the excitation energy. The calculations do not include the radiation damping channel [93], as it is negligible for $Z=5$ compared to the Auger decay term. Fano *q* parameters were not fitted since they are only physically meaningful for total cross sections. The total widths of the resonances could not be extracted from the measured cross sections due to the much larger spectrometer resolution (~0.5 eV).

4. Convolution with analyzer energy resolution

All *R*-matrix SDCS calculations were multiplied by the H_2 Compton profile and convoluted with the spectrograph's response function, given by a Gaussian with a FWHM of $0.000\,625\times W$ (eV) enabling a direct comparison to the data after using Eq. (3). The effect of different resolutions on the DDCS spectra is shown in Fig. 5. Clearly, the narrow minima will only be observable with comparable resolution.

C. Comparison with earlier work

The calculation of RTEA cross sections within the impulse approximation has undergone a few successive refinements as the field has matured. The first RTEA measurement assumed an isotropic angular distribution for the emission of the electrons [50]. It was later realized that the resonances produced by RTE with angular momentum *L* are strongly aligned and, therefore, the correct angular distribution must be $\sim|Y_{L,M_L=0}(\theta,0)|^2$ [23,53,94], which was soon verified experimentally [54]. Finally, it was clear from the Fano profile of the resonances that interference between the direct elastic and the resonant scattering amplitudes had to be introduced. Such a treatment was presented by Bhalla [6,55], who gave a cross-section expression that involved the coherent sum of the direct (nonresonant) and resonant amplitudes. However, for simplicity, he used only the Coulomb amplitude for the direct term, neglecting the short-range direct amplitude. For the resonant amplitude, he used the usual Lorentzian-like expression involving the Auger widths and resonant energies,

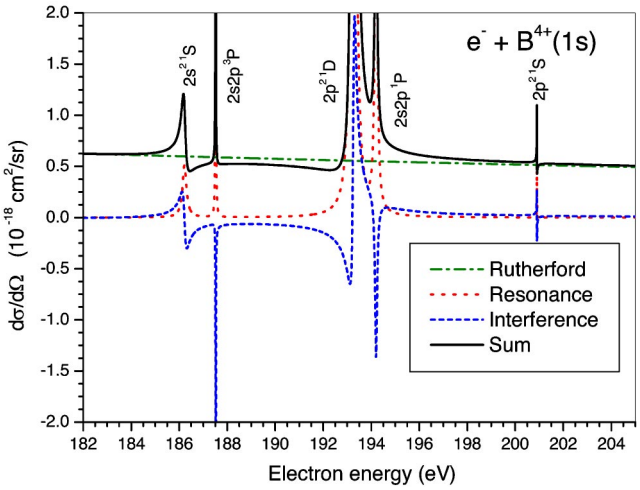

FIG. 6. (Color online) Calculated SDCS for 180° electron scattering from B^{4+} using the formulation of Ref. [6] with $Z=q=4$ and the Hartree-Fock Auger rates and widths given in Table II. Dashed-dot line: Rutherford term [Eq. (7)]; dotted line: resonance term; short dashed line: interference term [includes contributions from both C_I and A terms in Eq. (5) of Ref. [6]]; and continuous line: sum of all three terms. The resonance and interference terms are seen to have negligible nonresonant contributions as opposed to the full R-matrix calculations based on Eq. (6).

which were obtained from Hartree-Fock (HF) calculations [6]. The contributions from the direct Coulombic, resonant, and interference terms are shown in Fig. 6 for the case of 180° electron scattering from $B^{4+}(1s)$ using the HF rates given in Table II. In Fig. 7, comparison with our B^{4+} data and R-matrix calculations is shown which includes the convolution with the response function of the analyzer (see also Sec. IV B 4). The total SDCS in Fig. 6 is incomplete, of course, since the short-range, nonresonant amplitude (and its interference with the other amplitudes) has been neglected. As can be seen from Fig. 3, the full R-matrix calculation shows a significant contribution from the short-range, nonresonant amplitude, not only as an increase in the overall background cross section, but also in the additional interference effect. Bhalla recognized the shortcomings of this formulation and a bit later [64] adopted the R-matrix formula-

TABLE II. Auger transition energies ε_R(eV) and Auger rates $A_a(10^{13}\ s^{-1})$ of the $F^{7+}(2l2l')$, $B^{3+}(2l2l')$, and $B^{2+}(1s2l2l')$ intermediate states. The initial and final states are the $F^{8+}(1s)$, $B^{4+}(1s)$, and $B^{3+}(1s^2)$ ground states, respectively. Auger rates were obtained from the total widths Γ assuming $\hbar A_a \approx \Gamma$ since the radiative rates $A_r \ll A_a$ for these transitions. Γ was extracted from the R-matrix results (see text).

	ε_R			A_a		A_r
State	R matrix	HF	Expt.	R matrix	HF	HF
$B^{3+}(2s^2\ ^1S)$	186.14	186.22		29.61	29.88	0.033
$B^{3+}(2s2p\ ^3P)$	187.44	187.52		1.49	2.02	0.197
$B^{3+}(2p^2\ ^1D)$	193.26	193.53	193.26[a]	24.63	28.60	0.120
$B^{3+}(2s2p\ ^1P)$	193.89	194.20		13.41	15.91	0.065
$B^{3+}(2p\ ^1S)$	200.77	200.90		1.37	1.10	0.086
$C^{4+}(2p^2\ ^1D)$		273.3[b]			29.5[b]	0.148[b]
$N^{5+}(2p^2\ ^1D)$		366.9[b]			30.5[b]	0.267[b]
$O^{6+}(2p^2\ ^1D)$		474.2[b]			31.2[b]	0.456[b]
$F^{7+}(2p^2\ ^1D)$	594.38	595.0[b]	594.38[a]	30.36	31.8[b]	0.749[b]
$F^{7+}(2s2p\ ^1P)$	595.63			9.01		
$B^{2+}(1s2s^2\ ^2S)$	154.68		154.7±0.3	9.91		
$B^{2+}[1s(2s2p\ ^1P)^2P]$	161.10		161.2±0.4	0.85		
$B^{2+}[1s(2s2p\ ^3P)^2P]$	163.95		164.1±0.3	4.79		
$B^{2+}(1s2p^2\ ^2D)$	166.19		166.19[a]	6.85	8.60	
$B^{2+}(1s2p^2\ ^2S)$	171.39			1.34		

[a]Used for experimental energy calibration.
[b]Hartree-Fock (HF) calculations from Ref. [116].

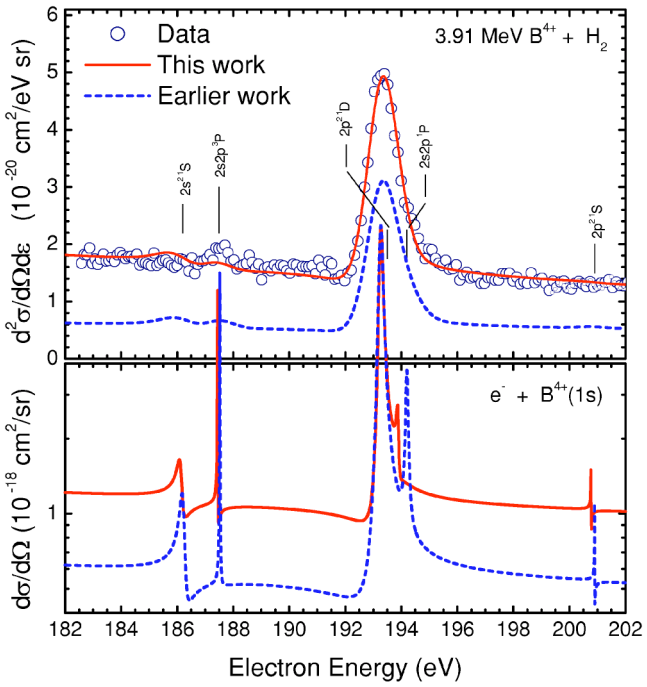

FIG. 7. (Color online) (Bottom) Comparison of the calculation shown in Fig. 6 and our *R*-matrix calculation for 180° electron scattering from B^{4+}. (Top) The DDCS spectrum is compared to the two calculations which were converted to DDCS using the electron scattering model formulation and after further convolution with the spectrometer resolution. The overall discrepancy between the two theoretical results is evident (see discussion in text).

tion based on the differential scattering code of Ref. [95].

From the above discussion, it is clear that only differential cross-section measurements based on the full scattering treatment [5] can be expected to provide a complete account of the interference structures. This information is partially lost when measuring total cross sections, as in a typical dielectronic recombination measurement in storage rings [8]. However, most of the interference structures, especially around the higher *KLn* resonances, are probably too sharp to be amenable to direct observation by electron spectroscopy. The interferences among the *KLL* resonances, though, as demonstrated by Fig. 5, are clearly within experimental limits. The present (rest frame) resolution of ~0.5 eV was obtained with a deceleration factor of $F=4$. A higher deceleration factor of $F=8$ was found to make only marginally small improvements to the HDA energy resolution, while cutting the size of the energy window by a factor of 2. For this reason, reported DDCS were taken only with $F=4$. Improved spectrometer performance in the future should enable higher-resolution measurements. Other inherent parameters that can limit the energy resolution include energy straggling of the ion beam [96] when post-stripper foils are used and kinematic line-broadening effects [46,97]. All the reported DDCS for B^{3+} beams were taken without the use of a post-stripper and therefore straggling was not an issue, except for B^{4+} beams where this effect was important, as it was for B^{3+} in the example shown in Fig. 14. Without post-stripping, the ultimate limit is imposed by the kinematic broadening, even at the preferential 0° observation angle utilized here [46,97–99]. For our present setup, this broadening is found to be smaller than 30 meV in the projectile rest frame when using a 4.0 MeV boron beam and is therefore also not a problem. For higher Z ions, though, which require a higher projectile energy for resonance conditions, both broadening effects could increase, eventually becoming a serious consideration. At nonzero observation angles ($\theta_L \gtrsim 1°$), the kinematic broadening is huge (about 100 times larger than at $\theta_L=0°$) [46], making high-resolution measurements practically impossible.

V. DATA ANALYSIS

A. Energy calibration of spectra

The electron spectra were energy calibrated with the use of a typical oscilloscope tube electron-gun, which was biased at a known set of negative voltages, measured with an accurate multimeter ($5\frac{1}{2}$ digit model Keithly 197), and the positions (ADC channel numbers) of the peaks were recorded. The electron gun was placed at the same location as the gas-cell in order to have the same focusing conditions. The relation between the laboratory electron energy ε_L and the corresponding channel number i has proven to be a smooth quadratic function of the form $\varepsilon_{L_i}=a+bi+ci^2$, where the parameters a, b, and c depend on the tuning energy W and the deceleration factor F [73]. The ion beam energies were accurately determined by aligning the $2p^2\ ^1D$ or $1s2p^2\ ^2D$ lines with the *R*-matrix calculations.

B. Determination of the absolute DDCS

The experimental DDCS for electron production in ion-atom collisions, for most of the detection systems using analyzers, is obtained from the well-known formula [100]

$$(\mathrm{DDCS}_i) \equiv \frac{d^2\sigma_i}{d\Omega_L\, d\varepsilon_{L_i}} = \frac{N_{e_i} t_{\mathrm{DTC}}}{N_I\, L_c\, n\, \Delta\Omega\, \Delta\varepsilon_{L_i}\, T\, \eta_i}, \quad (14)$$

where N_{e_i} is the number of electron counts in the ith channel. Typical values of the experimental setup parameters are given in Table I. A typical spectrum took between 20 and 60 min collection time. $\Delta\varepsilon_{L_i}$ is the energy step of the spectrum per channel i ($\Delta\varepsilon_{L_i}=b+2ci$). The overall transmission of the spectrograph, neglecting the two grids, was assumed to be 1, as it is governed by the analyzer entry aperture at the interface between analyzer and lens. The aperture's relatively large dimension ($d_0=6$ mm) compared to the dimension of the focusing image at the entrance of the analyzer (diameter $\leqslant 3$ mm according to SIMION electron optics [101,102] simulations) established a transmission of 100% over the entire energy acceptance window and was found to be independent of F (up to $F=8$) [73].

The PSD efficiency η_i depends mainly on the electron detection energy for the same PSD operating voltages. In our setup, the detection energy was fixed at the value of 1000 eV by appropriately floating the detector, thus resulting in a constant average efficiency value independent of W. The average efficiency value was determined by normalizing the 21.32 MeV $F^{8+}+H_2$ nonresonant (BEe) spectrum to the

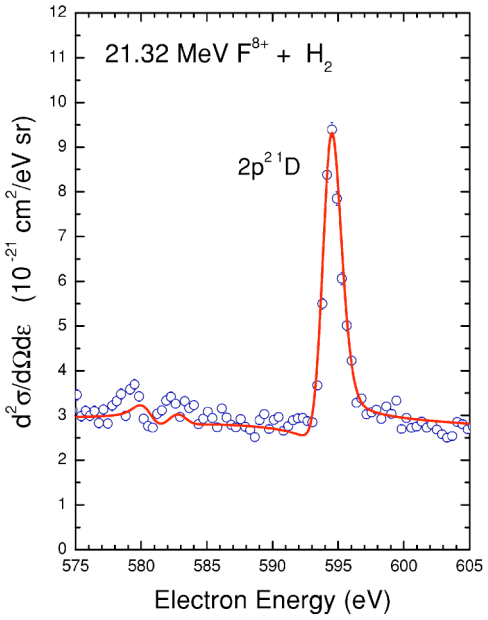

FIG. 8. (Color online) Projectile rest frame absolute electron DDCS for the 21.32 MeV $F^{8+}+H_2$ collisions system, near the $2p^2\,{}^1D$ resonance. Present *R*-matrix calculations, shown by the solid line, are seen to be in excellent agreement with the measurement.

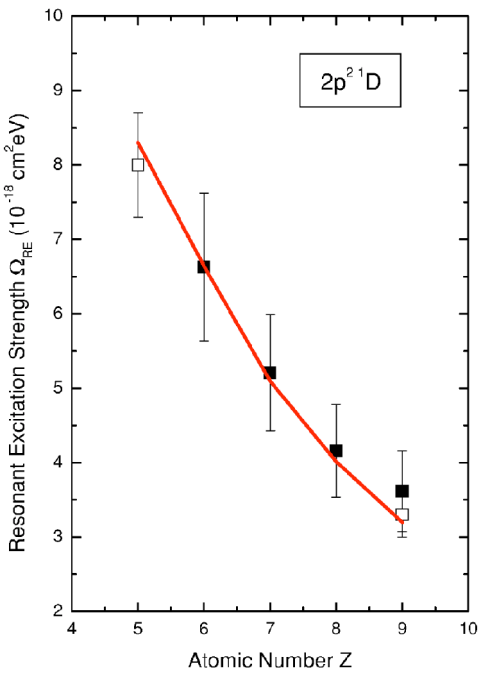

FIG. 9. (Color online) Resonance excitation collision strengths Ω_{RE} plotted as a function of atomic number Z for the $2p^2\,{}^1D$ resonance taken in collisions of H-like ions with H_2 targets. Open squares: present measurements; solid squares: values extracted from the older data of Toth *et al.* [58] taken with a two-stage slit spectrometer; line: Hartree-Fock calculation. Good agreement is seen for the common point of fluorine at $Z=9$.

ESM-*R*-matrix calculations, as it is known to be valid at these collision velocities [58]. An average efficiency of $\eta \approx 0.20$ was established in this way. We note that this procedure greatly reduces the overall absolute error in the DDCS since the possible individual absolute errors associated with the parameters L_c, n, $\Delta\Omega$, and T in Eq. (14) are all absorbed in the determination of η, thus reducing the otherwise overall error by almost a factor of 2. Thus, the overall absolute DDCS error can be expected to be around 10–15% [47], which explains the very nice agreement seen between theory and experiment throughout the spectrum. The absolute DDCSs obtained were finally transformed to the projectile rest frame according to the kinematic transformations [84]

$$\varepsilon = [\sqrt{\varepsilon_L} - \sqrt{t}]^2, \tag{15}$$

$$\frac{d^2\sigma(\varepsilon)}{d\Omega\, d\varepsilon} = \sqrt{\frac{\varepsilon}{\varepsilon_L}}\,\frac{d^2\sigma(\varepsilon_L)}{d\Omega_L\, d\varepsilon_L}, \tag{16}$$

valid for observation at $\theta_L = 0°$, which correspond to a scattering angle of $\theta = 180°$ in the projectile rest frame. The index L serves to identify quantities in the laboratory frame and $t = \frac{1}{2}V_p^2$ is the kinetic energy of an electron moving with the ion beam velocity V_p.

VI. RESULTS AND DISCUSSION

A. Consistency tests

In order to eliminate possible systematic uncertainties due to the spectrograph performance, the strong $2p^2\,{}^1D$ RE line formed in collisions of 21.32 MeV $F^{8+}+H_2$ was measured first. The excellent agreement between previous *R*-matrix calculations and experimental results for the cases of C, N, O, and F [58] favored the $2p^2\,{}^1D$ line as a benchmark for instrumental tests. The obtained DDCS spectrum and corresponding *R*-matrix results are shown in Fig. 8 in the projectile rest frame.

Present *R*-matrix calculations are seen to be in excellent agreement with the measurement (the broad nonresonant part was used for the efficiency determination). A direct comparison between the DDCS data of Ref. [58] was not possible due to the different energy resolutions. We therefore integrated the areas under the $2p^2\,{}^1D$ peak to extract SDCS from which RE collision strengths Ω_{RE} [23,55] were computed from Hartree-Fock calculated rates given in Table II. In Fig. 9 we compare the extracted Ω_{RE} from our F^{8+} and B^{4+} on H_2 measurements reported here to the Ω_{RE} values extracted from the older data (taken with a two-stage slit spectrometer) reported in Ref. [58]. As can be seen from the figure, all values lie well within the statistical uncertainties, thus establishing the reliability of our spectrograph.

B. $B^{4+}(1s)+H_2$: He-like resonances

Collisions with $B^{4+}(1s)$ ions were employed in the measurements as the simplicity of this system (ground-state hydrogenic ion) allows for a clear test of the ESM-*R*-matrix calculation. In Fig. 10, the data and calculations are shown for the 3.91 MeV $B^{4+}+H_2$ collision system. The He-like $2lnl'$ doubly excited states populated by RE and relaxing via Auger decay back to the $B^{4+}(1s)$ ground state are seen to be

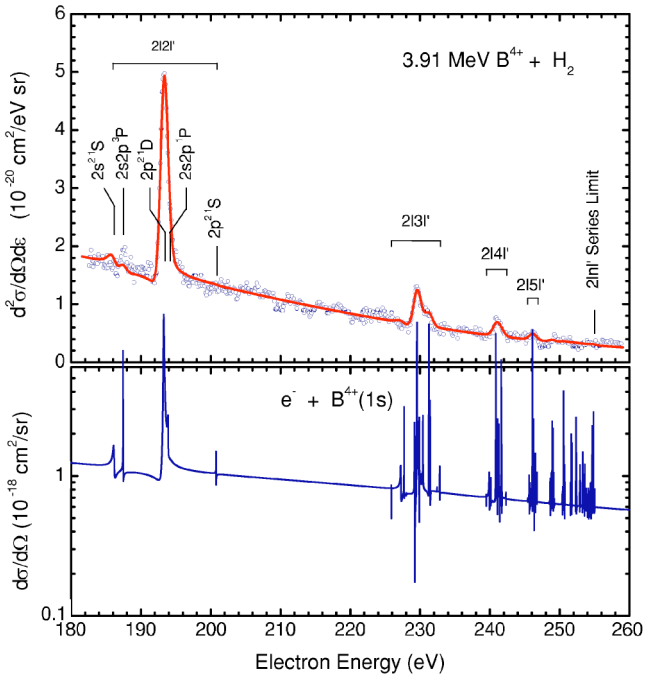

FIG. 10. (Color online) (Top) Data: Projectile frame DDCS electron spectra for 3.91 MeV $B^{4+}+H_2$ collisions. Solid line: ESM-*R*-matrix calculations [Eq. (3) and bottom] are seen to be in excellent agreement with the measurement. (Bottom) SDCS *R*-matrix calculations for 180° elastic electron scattering from $B^{4+}(1s)$ ions, plotted as a functions of the incident electron energy. The $B^{3+}(2lnl')$ resonances are seen superimposed on top of the broad nonresonant continuum.

superimposed on the broad nonresonant continuum (BEe peak). The manifolds for $n=2,3,4,5$ are well resolved. Even though the instrumental energy resolution was not adequate for resolving the Auger lines within each manifold for the $2lnl'$ ($n\geqslant 3$) states, an excellent overall agreement is established between the ESM-*R*-matrix calculations and the experiment. Interference effects primarily between the resonant and nonresonant parts are also evident in the case of the strong $2p^2\ ^1D$ line. The line's asymmetry, widely known as the *Fano profile* [103], is very well reproduced by the *R*-matrix calculations.

The excellent agreement between the ESM-*R*-matrix calculations and the measurements indicates that the IA still seems to be valid even for velocity ratios as low as $\nu=3.53$, thus lowering the previous limit of 4.44 which corresponded to the 6.75 MeV $C^{5+}+H_2$ collision system [58]. It would be of interest to push this limit to even lower values of ν by performing similar DDCS measurements with Be and Li ion beams. Eventually, for values of $\nu\sim 1$, the IA has been observed to break down, as already reported for electron DDCS measurements of 300 keV $He^+ + H_2$ [94] and $He^+ + He$ [78] collisions. For these collision systems, SDCS HF calculations of RTEA cross sections were found to be about six times larger than experiment [23] for reasons not yet clearly understood [104,105]. It would be of interest also to compare these results with *R*-matrix calculations at the DDCS level.

C. $B^{3+}(1s^2)+H_2$: Li-like resonances

The production of He-like ion beams from tandem Van de Graaff accelerators usually results in a non-negligible long-lived $1s2s\ ^3S$ metastable component, along with the main $1s^2\ ^1S$ ground-state part of the beam. The metastable component may complicate the Auger spectra by opening a number of excitation or capture channels not available for ground-state scattering. Moreover, the identification of the spectral lines may become problematic, if not impossible, when accidental overlapping manifolds from different decay channels occur [86]. Most important, the measurement of any absolute cross section with He-like ion beams requires the accurate determination of the metastable beam fraction. In the literature, RES measurements were reported for F^{7+} collisions with H_2 and He targets [56]. Theoretical predictions of the *KLL* SDCS showed discrepancies of ~20% with these measurements, a value well within the ~30% accuracy of the metastable fraction determined from older x-ray measurements [106,107].

In the case of boron, however, we have recently shown [69] that the production of B^{3+} ions after gas stripping inside the tandem accelerator at beam energies lower than 2 MeV results in significantly lower $1s2s\ ^3S$ metastable fractions compared to foil post-stripping at higher collision energies lower than 2 MeV. A method for determining this fraction partly based on theoretical cross sections for capture was also presented [69]. A similar method, but relying only on purely experimental procedures, was also developed [65]. Both techniques were found to give nearly identical results [108]. We used the second technique to determine the metastable fraction *in situ* to be $f_{3S}=3\pm 1\%$, which is indeed very small. Thus, in our reported DDCS measurements, the electron scattering data do not suffer from significant spectral complications and relative uncertainties arising from the metastable fraction determination.

In Fig. 11, the data and ESM-*R*-matrix calculations for the 4.00 MeV $B^{3+}+H_2$ collision system are shown. The observed ^4P state is primarily formed by $2p$ capture to the $1s2s\ ^3S$ state and is therefore not included in the *R*-matrix calculations. It cannot be populated by RE from the ground state, due to spin conservation considerations [56]. Electron capture to the $2p$ metastable core can also give rise to contributions to the $1s2s2p\ ^2P$ lines. Other inelastic contributions are also observed at Auger energies of 187.5 and 193.5 eV. These were identified as the $2s2p\ ^3P$ and $2s2p\ ^1P$ hollow ionic states, respectively, produced by $1s\rightarrow 2p$ excitation of the metastable core. All these contributions from the metastable core were investigated in more detail in the energy dependence study below.

1. Collisional energy dependence of DDCS

The agreement between the ESM-*R*-matrix calculations and the data in Fig. 11 is quite remarkable. Some substantial Fano interference structures are predicted by the calculations at 155 and 166 eV, but are only barely observable with the existing energy resolution. Contributions due to the small amount of metastable core have also been noted. To test the validity of the ESM at other collision velocities V_p, and also

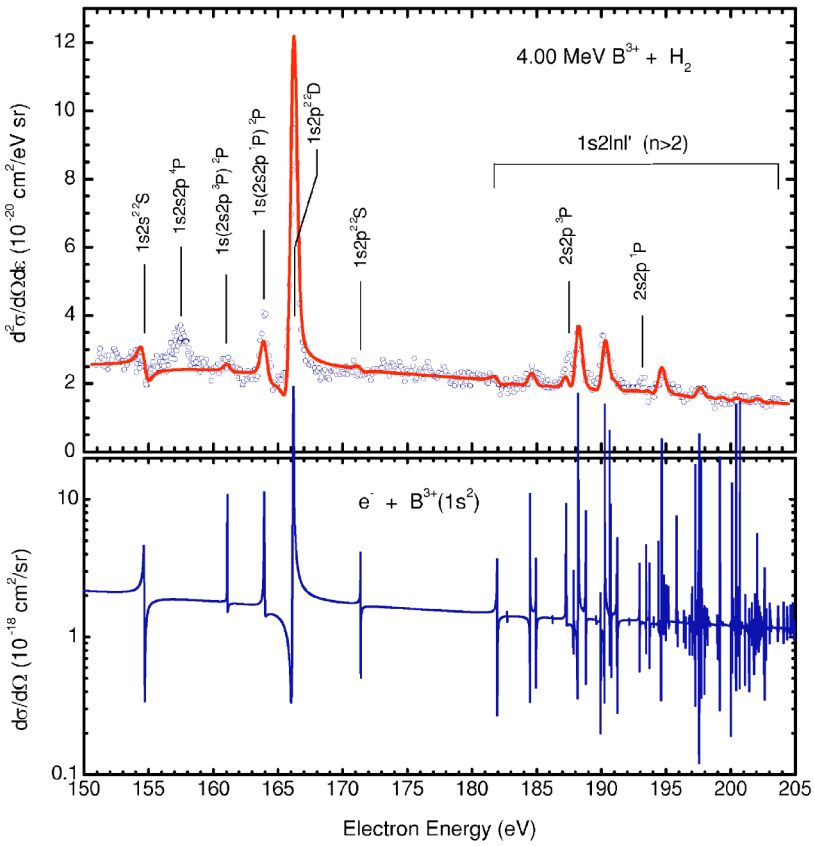

FIG. 11. (Color online) Same as in Fig. 10, but for 4.00 MeV $B^{3+}+H_2$ collisions. Now the $B^{2+}(1s2lnl')$ resonances produced by resonant electron scattering are seen to be superimposed on top of the broad nonresonant continuum (bottom). The presence of the $1s2s2p\ ^4P$ and $2s2p\ ^{3,1}P$ lines in the data is due to capture and excitation processes with the small contaminant ($\lesssim 3\%$) of $1s2s\ ^3S$ metastable ions not included in the *R*-matrix calculations.

to explore how background contributions from the metastable core change, we performed an energy dependence study. The observed resonances are expected to drop off rapidly as the Compton profile is moved across the resonances (see also Fig. 16 below). Electron capture should also gradually drop off with increasing projectile energy, while quasifree electron impact $1s \rightarrow 2p$ excitation of the metastable core should exhibit a threshold and eventually also fall off gradually with increasing collision energy. These features are well demonstrated in our 3.08–7.48 MeV (ν=3.10–4.83) study of the energy dependence of the DDCS. Both *KLL* and *KLn* ($n>2$) spectra were recorded for a set of six ion projectile energies covering the resonant excitation region. Each spectrum was recorded at a certain tuning energy *W* (no segment overlapping was necessary). The results are shown in Figs. 12 and 13 for the *KLL* and *KLn* cases, respectively. The nonresonant part (BEe contributions) was subtracted both from the theory and from the data to facilitate a more detailed graphical inspection of the resonances.

For the *KLL* case (see Fig. 12), theory reproduces the $1s2p^2\ ^2D$ resonance very nicely except at the lowest collision energy of 3.08 MeV, possibly signifying a departure from the IA at ν=3.10. The heights of the two ^2P lines are also seen to always be larger than theory for all collision energies. We note that the $1s(2s2p\ ^1P)^2P$ line may be highly affected by the presence of the neighboring $1s2p^2\ ^2D$ line, which shows a strong interference in the energy region between 163 and 170 eV. A detailed inspection of the *R*-matrix results shows that the interference terms between the Coulombic and short-range scattering amplitudes [the second term in Eq. (6)] for these lines are of opposite signs, negative for the ^2P and positive for the ^2D state, respectively (see Fig. 3). This would make this two-line combination particularly sensitive to interference. Our *R*-matrix results were found to be fairly insensitive to further inclusion of configuration interaction and pseudo-orbitals (optimized on the actual $1s2l2l'$ configuration) and therefore we rule out an unconverged theoretical description of the scattering processes as the cause for this discrepancy. The enhanced ^2P lines could *not* be due to RE contributions from the small $B^{3+}(1s2s\ ^3S)$ contaminant, since these energy levels lie above the $B^{2+}(1s2l2l')$ levels [56]. Another process which could also contribute to transfer and excitation, and therefore would have the same signature as RE, is nonresonant transfer and excitation (NTE) [105,109–112]. This process involves the excitation of a projectile electron due to the Coulomb influence of the target nucleus, with the simultaneous (but independent) capture of a target electron to some excited projectile state under the Coulomb influence of the projectile nucleus. Our *R*-matrix calculations refer only to electron scattering and therefore do not include any of the above background processes. However, NTE contributions are significantly reduced for low-*Z* targets such as H_2 [56] and are therefore expected to be small. Finally, it is improbable that these discrepancies, for example at 4.00 MeV, can be attributed to the breakdown of the IA, since we have already seen (in Fig. 10) that for the $B^{4+}+H_2$ system at the same collision energy (same ν), excellent agreement between theory and experiment is demonstrated.

2. Background processes involving the 1s2s ^3S metastable core

Electron capture to the metastable core can give rise to the $1s2s2p\ ^4P$ and $1s2s2p\ ^2P$ states. In fact, a ratio of 8:1:3 be-

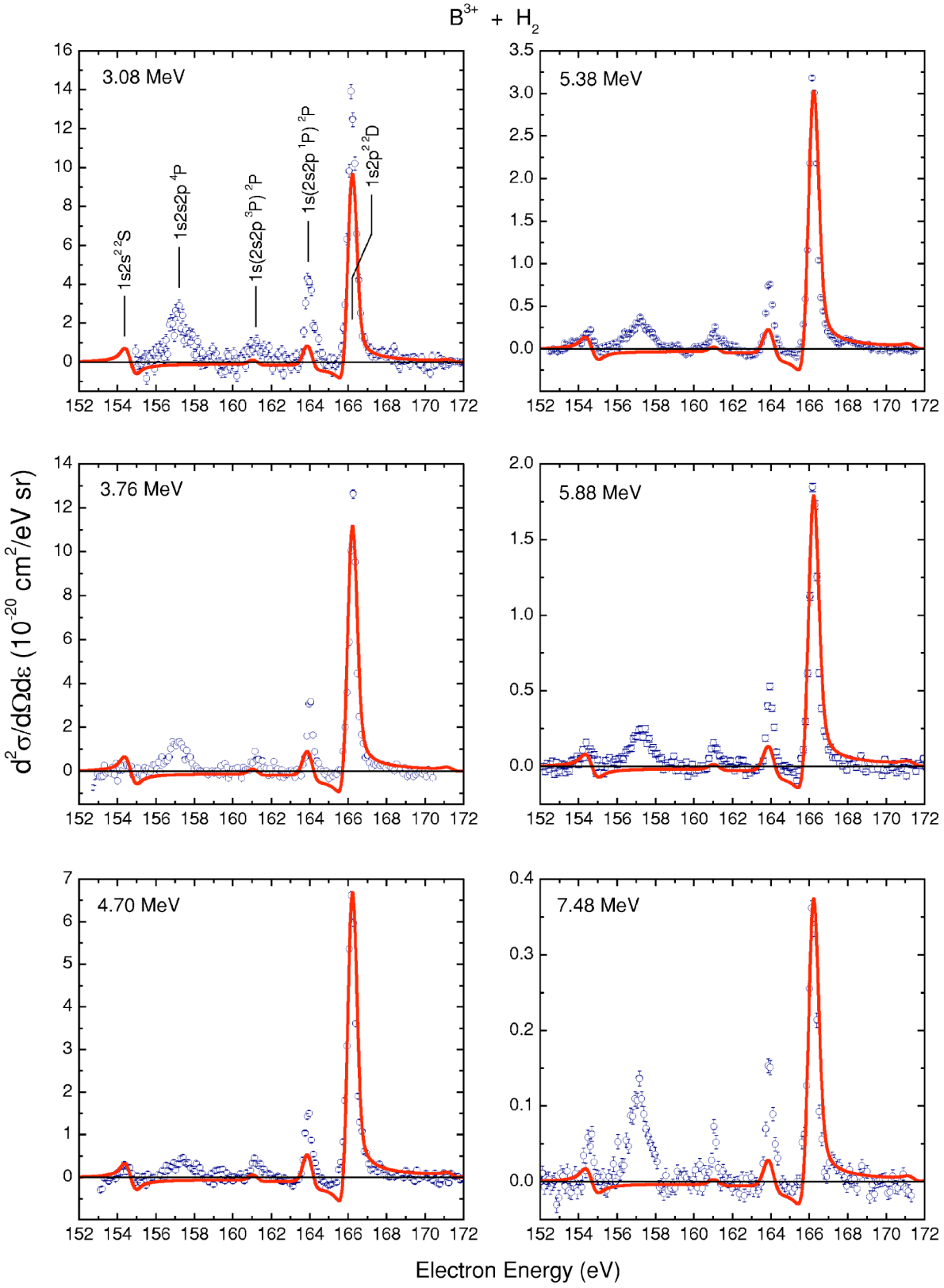

FIG. 12. (Color online) Energy dependence study of the *KLL* resonances produced in collisions of B^{3+} ions with H_2 gas targets. ESM–*R*-matrix calculations (solid lines) for $e^- + B^{3+}(1s^2)$ scattering are seen to reproduce very well the $1s2p^2\ ^2D$ resonance. The nonresonant contributions have been subtracted. The discrepancies observed around the ^2P resonances arise from $2p$ electron capture to the small amount of $1s2s\ ^3S$ component of the beam (see text).

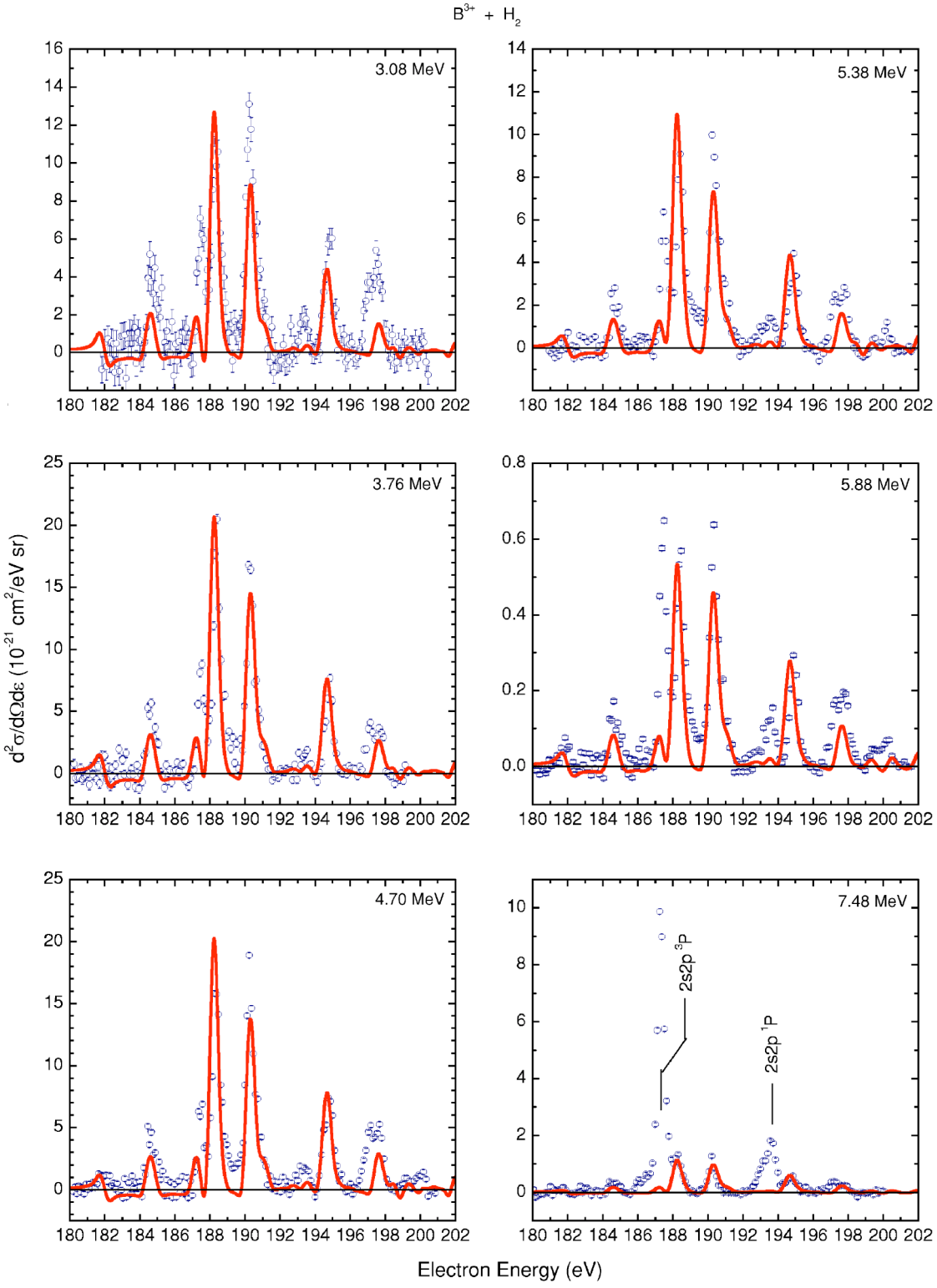

FIG. 13. (Color online) Same as in Fig. 12 but for the KLn $(n>2)$ spectral region. The agreement between the ESM–R-matrix calculations and the measurements is extremely good except at the lowest collision energy of 3.08 MeV. Unaccounted peaks are due to inelastic contributions primarily formed by $1s \rightarrow 2p$ excitation of the $1s2s\ ^3S$ metastable component of the beam, as, for example, those present at electron energies of 187.5 $(2s2p\ ^3P)$ and 193.5 $(2s2p\ ^1P)$ eV.

tween the capture probabilities to the respective $1s[2s2p(^3P)](^4P)$, $1s[2s2p(^3P)](^2P)$, and $1s[2s2p(^1P)](^2P)$ states can be mathematically deduced, as shown in the Appendix. First, the capture of a $2p$ electron to the $1s2s(^3S)$ core, once averaged over the magnetic quantum numbers of each, results through Clebsch-Gordon analysis in a 4/6 probability for populating the $1s2s(^3S)2p(^4P)$ state and a 2/6 probability for populating the $1s2s(^3S)2p(^2P)$ state. However, this latter state is not pure; the nearly pure states are the $1s[2s2p(^3P)](^2P)$ and $1s[2s2p(^1P)](^2P)$ states, since only the $n=2$ electrons correlate appreciably. A recoupling analysis shows that this captured $1s2s(^3S)2p(^2P)$ state is made up of 1/4 of the $1s[2s2p(^3P)](^2P)$ "pure" state and 3/4 of the $1s[2s2p(^1P)](^2P)$ "pure" state, hence the breakdown of the captured state into 8/12, 1/12, and 3/12 of the respective final states, in energy order.

To check the validity of the above prediction, we compared the DDCS for collisions with two He-like B^{3+} beams having a very different metastable content. The results are shown in Fig. 14. In the first case, the low metastable fraction ($f_{^3S} \lesssim 3\%$) resulted in negligible ^4P contributions, while in the second case ($f_{^3S}=25\%$), the ^4P contribution was large. Details on the metastable fraction production and determination can be found in Ref. [65]. In both cases we note the excellent agreement for the $1s2p^2\ ^2D$ state, which can be produced only from the ground state. The enhancement of the ^4P state is always accompanied with an enhancement of both ^2P peaks. Integrating the areas under the ^2P peaks in both the measured and *R*-matrix-ESM DDCS and then subtracting the theory from the experiment should give just the extra contributions due to capture. Indeed, the ratio between the $1s(2s2p\ ^3P)^2P$ and $1s(2s2p\ ^1P)^2P$ states was found to be 2.9 ± 0.4 after such a procedure. This result is in excellent agreement with the 3:1 ratio predicted by the model for the capture of a $2p$ electron to the $1s2s\ ^3S$ state already described. The $1s2s2p\ ^4P$ state was excluded from such an analysis due to complications arising from its long decay path having to do with its metastable nature [113]. An accurate cross-section determination of this line would require the modeling of the solid angle contributions throughout the ion path from the gas-cell to the entrance of the analyzer [33,46], including the difficult calculation of the focusing effects of the spectrograph lens. These effects are obvious in the much broader energy width of the ^4P line arising from different contributions along the ion's trajectory; the lens settings are optimized for focusing electrons emitted from within the gas-cell volume, while the larger acceptance angles at the shorter distances will introduce much larger kinematic broadenings.

In Fig. 13, the *KLn* ($n>2$) spectra are shown for different collision energies. The agreement between the calculations and the data is remarkable, although, it is difficult to proceed to a more detailed analysis due to the numerous states that contribute to the formation of the resonances as seen in Fig. 11 (bottom) and which cannot be resolved.

The $2s2p\ ^3P$ and the $2s2p\ ^1P$ hollow states present in the spectra at energies 187.5 eV and 193.5 eV, respectively, are primarily formed by electron-nucleus (*enE*) [21,114] or electron-electron (*eeE*) [21,28] $1s \rightarrow 2p$ excitation of the

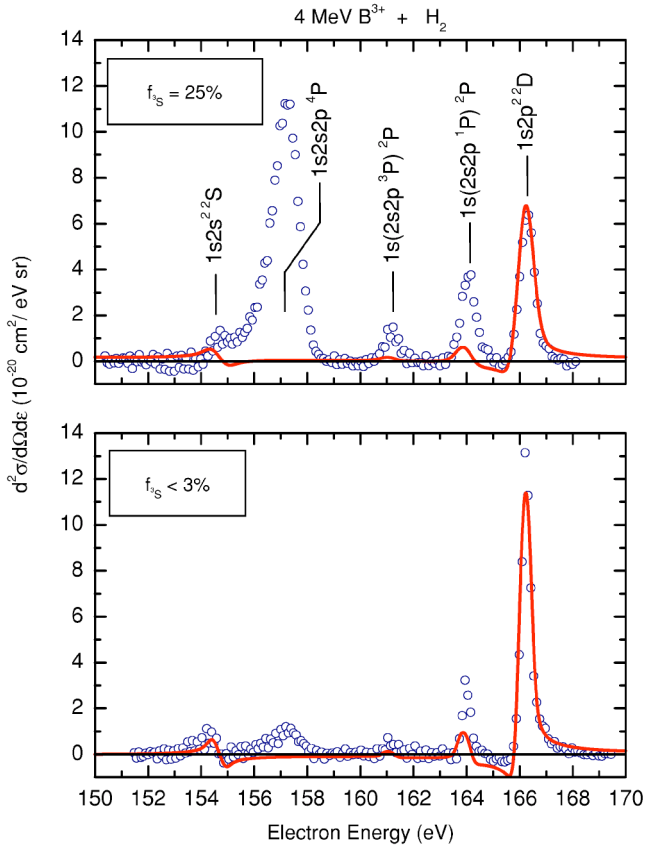

FIG. 14. (Color online) Experimental data (open circles) and ESM–*R*-matrix calculations (solid lines) for 4 MeV $B^{3+}+H_2$ collisions in the *KLL* spectral region. [Top] Metastable fraction $f_{^3S}=25\%$. [Bottom] $f_{^3S}<3\%$. The enhancement of the ^4P and ^2P lines in the case of $f_{^3S}=25\%$ is due to the capture of a $2p$ electron to the $1s2s\ ^3S$ ion core. For both spectra the electron analyzer was used with the same identical parameters. In the top spectrum, however, the lines are seen to be slightly broadened due to energy straggling of the boron ions in the carbon post-stripper foil utilized to produce a high metastable content. No post-stripping was used in the bottom spectrum. A spectrometer resolution of 0.59 eV and 0.35 eV was used, for the top and bottom spectrum, respectively.

$B^{3+}(1s2s\ ^3S)$ metastable core. The enhancement of these peaks for collision energies above 5 MeV is due to the crossing of the energy threshold for the $1s2s\ ^3S \rightarrow 2s2p\ ^{3,1}P$ *eeE* mechanism (5.02 and 5.15 MeV for ^3P and ^1P, respectively) [21]. Note that the $1s2s\ ^3S \rightarrow 2s2p\ ^1P$ excitation is succeeded via spin exchange between the target and the projectile electrons, respectively. For collision energies below the 5.15 MeV threshold for *eeE*, the process of transfer loss is also possible, similar to the case of $1s2s2p\ ^4P$ production in collisions of Li-like projectiles [28,115].

In Table II, the calculated and measured Auger energy transitions ε_R, and calculated Auger rates A_a, of the $F^{7+}(2l2l')$, $B^{3+}(2l2l')$ and $B^{2+}(1s2l2l')$ intermediate states are given. Data for the $2p^2\ ^1D$ state from Refs. [58,116] are also included for the sake of completeness.

3. Determination of IA-BEe enhancement factors

A very useful application of the IA is the determination of the absolute electron detection efficiencies η. These can be

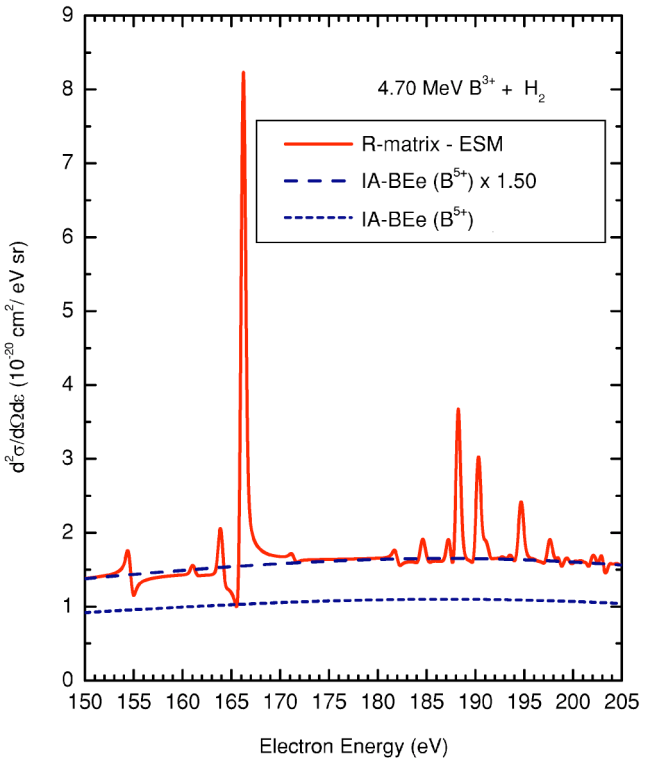

FIG. 15. (Color online) Scaling of Coulomb DDCS: The IA-BEe calculations for bare boron (B^{5+}) computed from the Coulomb formula [Eq. (7)] (short dashed line) are multiplied by the enhancement factor $\mathcal{R}=1.50$ (dashed line) to match the *R*-matrix results (solid line) over the nonresonant part of the DDCS spectrum.

safely determined by normalizing the data to the nonresonant part of the elastic scattering (BEe peak) [40,46,56,81]. Traditionally, in BEe calculations, the DDCS is obtained through the Coulomb scattering formula for a bare ion [utilized within the IA, i.e., Eq. (3)], multiplied by an overall enhancement factor $\mathcal{R}$ to account for any ionic structure [84]. Given the simplicity of the calculation and the accuracy of the result, enhancement factors become important information for absolute efficiency determination. In Fig. 15, an example of an *R*-matrix and IA-BEe calculations corrected for the enhancement factor is given. The agreement in the nonresonant DDCS is more than adequate for efficiency determination purposes. In Table III, we give the enhancement factors for the cases of F^{8+}, B^{4+}, and B^{3+} as determined by comparing the ESM–*R*-matrix and bare ion Coulomb calculations. The enhancement factors are in general dependent on the ion-beam energy. However, in the small interval of energies of our measurements, no significant change was observed.

TABLE III. IA-BEe overall enhancement factor $\mathcal{R} \equiv d^2\sigma(q)/d^2\sigma(Z)$ showing the enhancement of the DDCS for an ion with charge state *q* over that of a bare ion.

Ion	$\mathcal{R}$
$F^{8+}(1s)$	1.17
$B^{4+}(1s)$	1.25
$B^{3+}(1s^2)$	1.50

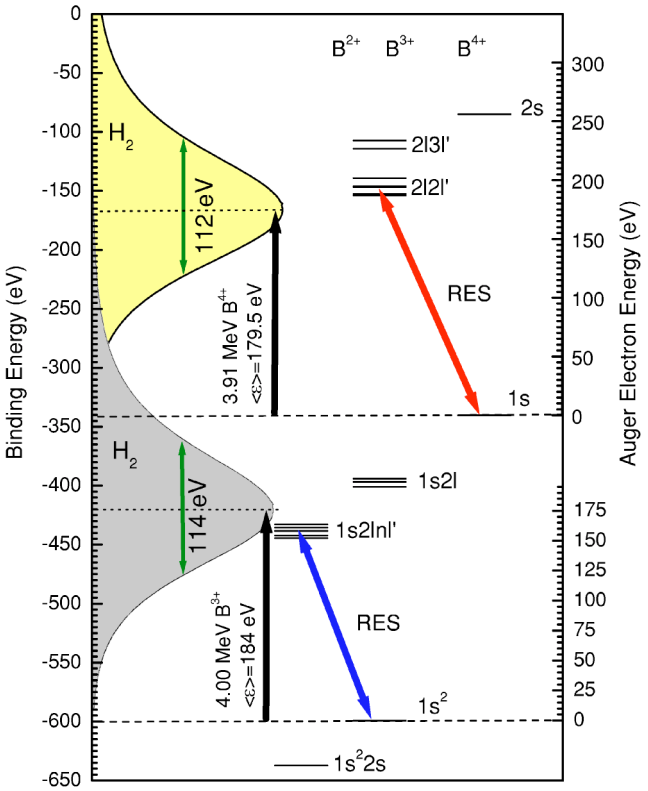

FIG. 16. (Color online) Boron energy level diagram: RES from $B^{4+}(1s)$ leads to $B^{3+}(2l2l')$ doubly excited states and from $B^{3+}(1s^2)$ leads to $B^{2+}(1s2lnl')$ doubly excited states. The quasifree electron "beam" spectral profiles in 3.91 MeV B^{3+} and 4.00 MeV B^{4+} (shaded areas) have a mean electron "beam" energy [see Eq. (2) with $p_z=0$] of $\langle\varepsilon\rangle=179.5$ and 184 eV, respectively, above each of the initial states with a broad FWHM of more than 100 eV, seen to overlap many resonances. The corresponding Auger electron energies for transitions to the ground state are given on the right-hand scale.

4. Effect of the Compton profile

We finally emphasize an important aspect of the technique of quasifree electron scattering. The effective *broad* energy distribution of the quasifree electron "beam" (about 100 eV in FWHM for an H_2 target) is actually *advantageous* [42,67]. Particularly in measuring DDCS, the whole series of RE states can be brought into resonance *simultaneously* at a collision energy of ~4 MeV [see Eq. (3)] [albeit with some minor reduction in intensity, as dictated by the Compton profile $J(p_z)$], thus avoiding the need for time-consuming energy scanning. In storage ring electron-ion merged-beam measurements, high resolution is used in defining the initial electron-beam energy. In our experiments, high resolution is used in measuring the final scattered electrons. In both cases, selectivity is provided either in the entrance or in the exit channel. The situation is illustrated in Fig. 16. Increasing the ion-beam energy results in the "sliding" of the Compton profile across the RE states in the energy-level diagram [42].

Thus, the RES line intensities will vary as a function of the beam energy as seen in the experimental data and calculations of Figs. 12 and 13 due to the changing relative probability of finding an incident electron at the resonant energy. Furthermore, as $J(p_z)$ is just an overall scaling factor within the ESM [Eq. (3)], no deconvolution of its influence on the DDCS is needed, as in the case of excitation or ionization measurements [21].

VII. SUMMARY AND CONCLUSION

In this investigation, we have presented the most extensive tests of elastic differential electron-ion scattering, to date, by measuring absolute DDCS for quasifree electron backscattering from ground-state He-like and H-like boron ions over the energy range of 150–260 eV covering all $1s2lnl'$ and $2l2l'$ resonances up to the series limit. A high-efficiency, zero-degree Auger projectile spectrograph, combined with a novel technique to obtain practically pure ground-state He-like boron ions, allowed for accurate DDCS measurements. A detailed presentation of the free-electron SDCS and a comparison with earlier models clearly showed some of the problems associated with the older formulations primarily affecting the angular distribution of the electrons which can be substantially modified from interference effects and the inclusion of more than one partial wave. *R*-matrix calculations for elastic, resonant, and nonresonant 180° differential cross sections for scattering of electrons from boron ions were found to be in excellent overall agreement when combined with the electron scattering model and the impulse approximation representing a milestone in the testing of the ESM. The ESM is important, as it provides a simple and general framework for linking electron scattering processes in the two rather distinct fields of ion-atom and ion-electron collisions [21]. These results add to the mounting evidence [10,41] that quasifree electron scattering, combined with high-resolution Auger projectile spectroscopy techniques, can be used to obtain unique, large-angle scattering DDCS of electrons from HCI. Since such measurements cannot be readily performed by conventional crossed or merged electron-ion differential scattering experiments, they presently provide the only viable technique for testing *differential* electron-ion scattering calculations, particularly in the sensitive large-angle scattering regime. In the future, after improving the differential pumping of our gas target, we plan to use Li^+ and Li^{2+} beams to extend our investigations to even lower values of ν and also introduce many-electron targets in both the ground state [117] and in highly excited Rydberg states for which the validity of the ESM is not yet clear.

ACKNOWLEDGMENTS

This work was supported by the Division of Chemical Sciences, Geosciences and Biosciences, Office of Basic Energy Sciences, Office of Science, U.S. Department of Energy. T.W.G. was supported in part by NASA Space Astrophysics Research and Analysis Program Grant No. NAG5-10445.

APPENDIX: PROBABILITY OF $2p$ CAPTURE TO THE $1s2s2p$ CONFIGURATION

In this appendix, we show how the capture of a $2p$ electron to a $1s2s(^3S)$ ion results in an 8:1:3 ratio of probabilities to the $1s[2s2p(^3P)](^4P)$, $1s[2s2p(^3P)](^2P)$, and $1s[2s2p(^1P)](^2P)$ states, respectively. We first have a $1s$ electron, with spin and magnetic quantum numbers $s_1=\frac{1}{2}$ and m_1, coupled to a $2s$ electron, with spin and magnetic quantum numbers $s_2=\frac{1}{2}$ and m_2, to yield a coupled $1s2s(^3S)$ state with quantum numbers $s_{12}=1$ and m_{12}, denoted as the ket vector

$$|s_{12},m_{12}\rangle = \sum_{m_1+m_2=m_{12}} C^{s_1\ s_2\ s_{12}}_{m_1\ m_2\ m_{12}} |s_1,m_1\rangle|s_2,m_2\rangle. \quad \text{(A1)}$$

The averaged, uncoupled, captured state $1s2s(^3S)2p$ can be denoted as

$$\begin{aligned}|[1s2s(^3S)]2p(^{2s+1}P)\rangle &= \frac{1}{\sqrt{(2s_{12}+1)(2s_3+1)}} \\ &\quad\times \sum_{m_{12},m_3} |s_{12},m_{12}\rangle|s_3,m_3\rangle \\ &= \frac{1}{\sqrt{(2s_{12}+1)(2s_3+1)}} \\ &\quad\times \sum_{m_{12},m_3} \sum_{s} C^{s_{12}\ s_3\ s}_{m_{12}\ m_3\ m} |s,m\rangle \\ &= \frac{1}{\sqrt{(2s_{12}+1)(2s_3+1)}} \\ &\quad\times \sum_{s} \sum_{m=-s}^{m=s} \sum_{m_{12}+m_3=m} C^{s_{12}\ s_3\ s}_{m_{12}\ m_3\ m} |s,m\rangle,\end{aligned} \quad \text{(A2)}$$

with $s_3=\frac{1}{2}$ and $s=2,4$. The probability of ending up in a state with final spin s is therefore given as

$$\begin{aligned}P(s) &= \frac{1}{(2s_{12}+1)(2s_3+1)} \sum_{m=-s}^{m=s} \sum_{m_{12}+m_3=m} (C^{s_{12}\ s_3\ s}_{m_{12}\ m_3\ m})^2 \\ &= \frac{1}{(2s_{12}+1)(2s_3+1)} \sum_{m=-s}^{m=s} 1 \\ &= \frac{2s+1}{6} \\ &= \begin{cases} 4/6 \text{ for the } [1s2s(^3S)]2p(^4P) \text{ state} \\ 2/6 \text{ for the } [1s2s(^1S)]2p(^2P) \text{ state,}\end{cases}\end{aligned} \quad \text{(A3)}$$

i.e., it breaks down according to spin statistics. The orthogonal property of the Clebsch-Gordon coefficients is used in the first step.

The captured doublet state $[1s2s(^1S)]2p(^2P)$ is not pure, but can be recoupled from a $\{[(s_1,s_2)s_{12}],s_3\}s$ coupling scheme to a $\{s_1,[(s_2,s_3)s_{23}]\}s$ one, where $s_{23}=1$ for the $1s[2s2p(^3P)](^2P)$ state and $s_{23}=0$ for the $1s[2s2p(^1P)](^2P)$ state. These latter states are essentially pure due to the domi-

nance of the correlation between the $n=2$ electrons. The initially captured $[1s2s(^1S)]2p(^2P)$ state can thus be written as

$$|\{[(s_1,s_2)s_{12}],s_3\}s\rangle = \sum_{s_{23}} (-1)^{s_1+s_2+s_3+s}\sqrt{(2s_{12}+1)(2s_{23}+1)} \times \begin{Bmatrix} s_1 & s_2 & s_{12} \\ s_3 & s & s_{23} \end{Bmatrix} |\{s_1,[(s_2,s_3)s_{23}]\}s\rangle, \tag{A4}$$

and the probability of populating the state with spin s_{23} is thus

$$P(s_{23}) = (2s_{12}+1)(2s_{23}+1)\begin{Bmatrix} s_1 & s_2 & s_{12} \\ s_3 & s & s_{23} \end{Bmatrix}^2 = 3(2s_{23}+1)\begin{Bmatrix} 1/2 & 1/2 & 1 \\ 1/2 & 1/2 & s_{23} \end{Bmatrix}^2 = \begin{cases} 1/4 \text{ for the } 1s[2s2p(^3P)](^2P) \text{ state} \\ 3/4 \text{ for the } 1s[2s2p(^1P)](^2P) \text{ state,} \end{cases} \tag{A5}$$

which does *not* follow from spin statistics. This gives a final breakdown of 8:1:3 between the energy-ordered states.

[1] I. D. Williams, Rep. Prog. Phys. **62**, 1431 (1999).
[2] B. A. Huber, C. Ristori, C. Guet, D. Küchler, and W. R. Johnson, Phys. Rev. Lett. **73**, 2301 (1994).
[3] J. B. Greenwood, I. D. Williams, and P. McGuinness, Phys. Rev. Lett. **75**, 1062 (1995).
[4] C. Bélenger, P. Defrance, R. Friedlein, C. Guet, D. Jalabert, M. Maurel, C. Ristori, J. C. Rocco, and B. A. Huber, J. Phys. B **29**, 4443 (1996).
[5] D. C. Griffin and M. S. Pindzola, Phys. Rev. A **42**, 248 (1990).
[6] C. P. Bhalla, Phys. Rev. Lett. **64**, 1103 (1990).
[7] L. H. Andersen, P. Hvelplund, H. Knudsen, and P. Kvistgaard, Phys. Rev. Lett. **62**, 2656 (1989).
[8] G. Kilgus *et al.*, Phys. Rev. Lett. **64**, 737 (1990).
[9] G. Kilgus, D. Habs, D. Schwalm, A. Wolf, R. Schuch, and N. R. Badnell, Phys. Rev. A **47**, 4859 (1993).
[10] A. Müller, in *Atomic and Molecular Data and their Applications*, edited by D. R. Schultz, P. S. Krstic, and F. Ownby, AIP Conf. Proc. No. 636 (AIP, Melville, NY, 2002), Vol. 73, pp. 202–212.
[11] A. Chutjian, A. Z. Msezane, and R. J. W. Henry, Phys. Rev. Lett. **50**, 1357 (1983).
[12] A. Chutjian, Phys. Rev. A **29**, 64 (1984).
[13] I. D. Williams, A. Chutjian, and R. J. Mawhorter, J. Phys. B **19**, 2189 (1986).
[14] B. A. Huber, C. Ristori, P. A. Hervieux, M. Maurel, C. Guet, and H. J. Andrä, Phys. Rev. Lett. **67**, 1407 (1991).
[15] X. Q. Guo, E. W. Bell, J. S. Thompson, G. H. Dunn, M. E. Bannister, R. A. Phaneuf, and A. C. H. Smith, Phys. Rev. A **47**, R9 (1993).
[16] D. C. Griffin, M. S. Pindzola, T. W. Gorczyca, and N. R. Badnell, Phys. Rev. A **51**, 2265 (1995).
[17] B. Srigengan, I. D. Williams, and W. R. Newell, J. Phys. B **29**, L605 (1996).
[18] N. Stolterfoht, Phys. Scr. **42**, 192 (1990).
[19] N. Stolterfoht, Nucl. Instrum. Methods Phys. Res. B **53**, 477 (1991).
[20] T. J. M. Zouros, D. H. Lee, J. M. Sanders, and P. Richard, Nucl. Instrum. Methods Phys. Res. B **79**, 166 (1993).
[21] T. J. M. Zouros, Comments At. Mol. Phys. **32**, 291 (1996).
[22] J. A. Tanis, in *Recombination of Atomic Ions*, edited by W. G. Graham, W. Fritsch, Y. Hahn, and J. Tanis, NATO Advanced Study Institute Series B: Physics (Plenum Publishing Corporation, New York, 1992), Vol. 296, pp. 241–257.
[23] T. J. M. Zouros, in *Recombination of Atomic Ions* (Ref. [22]), pp. 271–300.
[24] M. Kleber and D. H. Jakubaßa, Nucl. Phys. A **252**, 152 (1975).
[25] D. H. Jakubaba-Amundsen, J. Phys. B **20**, 325 (1987).
[26] T. Stöhlker *et al.*, Phys. Rev. A **51**, 2098 (1995).
[27] T. Stöhlker *et al.*, Phys. Rev. Lett. **86**, 983 (2001).
[28] T. J. M. Zouros, D. H. Lee, and P. Richard, Phys. Rev. Lett. **62**, 2261 (1989).
[29] B. Sulik, S. Ricz, I. Kádár, G. Xiao, G. Schiwietz, K. Sommer, P. Grande, R. Köhrbrück, M. Grether, and N. Stolterfoht, Phys. Rev. A **52**, 387 (1995).
[30] B. Sulik, S. Ricz, I. Kádár, G. Xiao, G. Schiwietz, K. Sommer, R. Köhrbrück, M. Grether, and N. Stolterfoht, Nucl. Instrum. Methods Phys. Res. B **98**, 262 (1995).
[31] H. P. Hülskötter, W. E. Meyerhof, E. Dillard, and N. Guardala, Phys. Rev. Lett. **63**, 1938 (1989).
[32] M. B. Shah, and H. B. Gilbody, J. Phys. B **24**, 977 (1991).
[33] D. H. Lee, T. J. M. Zouros, J. M. Sanders, P. Richard, J. M. Anthony, Y. D. Wang, and J. H. McGuire, Phys. Rev. A **46**, 1374 (1992).
[34] E. C. Montenegro, W. S. Melo, W. E. Meyerhof, and A. G. de Pinho, Phys. Rev. Lett. **69**, 3033 (1992).
[35] E. C. Montenegro, W. S. Melo, W. E. Meyerhof, and A. G. de Pinho, Phys. Rev. A **48**, 4259 (1993).
[36] E. C. Montenegro and T. J. M. Zouros, Phys. Rev. A **50**, 3186 (1994).
[37] W. Wu *et al.*, Phys. Rev. Lett. **72**, 3170 (1994).
[38] D. Brandt, Phys. Rev. A **27**, 1314 (1983).
[39] J. M. Feagin, J. S. Briggs, and T. M. Reeves, J. Phys. B **17**, 1057 (1984).
[40] D. H. Lee, P. Richard, T. J. M. Zouros, J. M. Sanders, J. L. Shinpaugh, and H. Hidmi, Phys. Rev. A **41**, 4816 (1990).
[41] P. Richard, C. P. Bhalla, S. Hagmann, and P. A. Závodszky, Phys. Scr., T **T80**, 87 (1999).
[42] P. Hvelplund, A. D. Gonzalez, P. Dahl, and C. P. Bhalla, Phys. Rev. A **49**, 2535 (1994).
[43] C. Kelbch, S. Hagmann, S. Kelbch, R. Mann, R. E. Olson, S. Schmidt, and H. Schmidt-Böcking, Phys. Lett. A **139**, 304 (1989).
[44] P. Richard, D. H. Lee, T. J. M. Zouros, J. M. Sanders, and J. L. Shinpaugh, J. Phys. B **23**, L213 (1990).
[45] M. E. Rudd, Y. K. Kim, D. H. Madison, and T. J. Gay, Rev.

Mod. Phys. **64**, 441 (1992).
[46] T. J. M. Zouros and D. H. Lee, in *Accelerator-based Atomic Physics Techniques and Applications*, edited by S. M. Shafroth and J. C. Austin (AIP, Woodbury, NY, 1997), pp. 426–479.
[47] N. Stolterfoht, R. D. Dubois, and R. D. Rivarola, *Electron Emission in Heavy Ion-Atom Collisions*, Springer Series on Atoms and Plasmas (Springer, Heidelberg, 1997).
[48] U. Bechthold, S. Hagmann, J. Ullrich, B. Bathelt, A. Bohris, R. Moshammer, U. Ramm, C. P. Bhalla, G. Kraft, and H. Schmidt-Böcking, Phys. Rev. Lett. **79**, 2034 (1997).
[49] C. Liao, S. Hagmann, C. P. Bhalla, S. R. Grabbe, C. L. Cocke, and P. Richard, Phys. Rev. A **59**, 2773 (1999).
[50] J. K. Swenson, Y. Yamazaki, P. D. Miller, H. F. Krause, P. F. Dittner, P. L. Pepmiller, S. Datz, and N. Stolterfoht, Phys. Rev. Lett. **57**, 3042 (1986).
[51] T. J. M. Zouros, D. H. Lee, P. Richard, J. M. Sanders, J. L. Shinpaugh, S. L. Varghese, K. R. Karim, and C. P. Bhalla, Phys. Rev. A **40**, 6246 (1989).
[52] B. D. DePaola, R. Parameswaran, and W. J. Axmann, Phys. Rev. A **41**, 6533 (1990).
[53] T. J. M. Zouros, C. P. Bhalla, D. H. Lee, and P. Richard, Phys. Rev. A **42**, 678 (1990).
[54] M. Benhenni, S. M. Shafroth, J. K. Swenson, M. Schulz, J. P. Giese, H. Schöne, C. R. Vane, P. F. Dittner, and S. Datz, Phys. Rev. Lett. **65**, 1849 (1990).
[55] R. Parameswaran, C. P. Bhalla, B. P. Walch, and B. D. DePaola, Phys. Rev. A **43**, 5929 (1991).
[56] D. H. Lee, P. Richard, J. M. Sanders, T. J. M. Zouros, J. L. Shinpaugh, and S. L. Varghese, Phys. Rev. A **44**, 1636 (1991).
[57] P. A. Závodszky, G. Tóth, S. R. Grabbe, T. J. M. Zouros, P. Richard, C. P. Bhalla, and J. A. Tanis, J. Phys. B **32**, 4425 (1999).
[58] G. Toth, P. A. Závodszky, C. P. Bhalla, P. Richard, S. Grabbe, and H. Aliabadi, Phys. Scr., T **T92**, 272 (2001).
[59] P. A. Závodszky, H. Aliabadi, C. P. Bhalla, P. Richard, G. Tóth, and J. A. Tanis, Phys. Rev. Lett. **87**, 033202 (2001).
[60] A. S. Alnaser, A. L. Landers, D. J. Pole, S. Hossain, O. A. Haija, T. W. Gorczyca, J. A. Tanis, and H. Knutson, Phys. Rev. A **65**, 042709 (2002).
[61] M. Kuzel, R. D. DuBois, R. Maier, O. Heil, D. H. Jakubassa-Amundsen, M. W. Lucas, and K.-O. Groeneveld, J. Phys. B **27**, 1993 (1994).
[62] M. W. Lucas, D. H. Jakubaßa-Amundsen, M. Kuzel, and K. O. Groeneveld, Int. J. Mod. Phys. A **12**, 305 (1997).
[63] T. J. M. Zouros, E. P. Benis, T. W. Gorczyca, A. D. González, M. Zamkov, and P. Richard, Nucl. Instrum. Methods Phys. Res. B **205**, 58 (2003).
[64] C. P. Bhalla, S. R. Grabbe, and A. K. Bhatia, Phys. Rev. A **52**, 2109 (1995).
[65] E. P. Benis, M. Zamkov, P. Richard, and T. J. M. Zouros, Phys. Rev. A **65**, 064701 (2002).
[66] M. Zamkov, E. P. Benis, P. Richard, and T. J. M. Zouros, Phys. Rev. A **65**, 062706 (2002).
[67] T. J. M. Zouros, E. P. Benis, and T. W. Gorczyca, Phys. Rev. A **68**, 010701(R) (2003).
[68] E. P. Benis, Ph.D. dissertation, Dept. of Physics, University of Crete (2001), (unpublished).
[69] M. Zamkov, H. Aliabadi, E. P. Benis, P. Richard, H. Tawara, and T. J. M. Zouros, Phys. Rev. A **64**, 052702 (2001).
[70] M. Zamkov, H. Aliabadi, E. P. Benis, P. Richard, H. Tawara, and T. J. M. Zouros, Phys. Rev. A **65**, 032705 (2002).
[71] T. J. M. Zouros and E. P. Benis, J. Electron Spectrosc. Relat. Phenom. **125**, 221 (2002).
[72] E. P. Benis and T. J. M. Zouros, Nucl. Instrum. Methods Phys. Res. A **440**, 462 (2000).
[73] E. P. Benis and T. J. M. Zouros, J. Electron Spectrosc. Relat. Phenom. (to be published).
[74] E. P. Benis, K. Zaharakis, M. M. Voultsidou, T. J. M. Zouros, M. Stöckli, P. Richard, and S. Hagmann, Nucl. Instrum. Methods Phys. Res. B **146**, 120 (1998).
[75] E. P. Benis, T. J. M. Zouros, and P. Richard, Nucl. Instrum. Methods Phys. Res. B **154**, 276 (1999).
[76] E. P. Benis, T. J. M. Zouros, H. Aliabadi, and P. Richard, Phys. Scr., T **T80**, 529 (1999).
[77] D. H. Lee, T. J. M. Zouros, J. M. Sanders, J. L. Shinpaugh, T. N. Tipping, S. L. Varghese, B. D. DePaola, and P. Richard, Nucl. Instrum. Methods Phys. Res. B **40/41**, 1229 (1989).
[78] A. Itoh, T. J. M. Zouros, D. Schneider, U. Stettner, W. Zeitz, and N. Stolterfoht, J. Phys. B **18**, 4581 (1985).
[79] F. Biggs, L. B. Mendelsohn, and J. B. Mann, At. Data Nucl. Data Tables **16**, 201 (1975).
[80] J. S. Lee, J. Chem. Phys. **66**, 4906 (1977).
[81] T. J. M. Zouros, G. Toth, P. Richard, C. Liao, and S. Hagmann, Nucl. Instrum. Methods Phys. Res. B **107**, 87 (1996).
[82] U. Bechthold, J. Ullrich, U. Ramm, G. Kraft, S. Hagmann, D. R. Schultz, C. O. Reinhold, and H. Schmidt-Böcking, Phys. Rev. A **58**, 1971 (1998).
[83] T. J. M. Zouros, P. Richard, K. L. Wong, H. I. Hidmi, J. M. Sanders, C. Liao, S. Grabbe, and C. P. Bhalla, Phys. Rev. A **49**, R3155 (1994).
[84] T. J. M. Zouros, K. L. Wong, S. Grabbe, H. I. Hidmi, P. Richard, E. C. Montenegro, J. M. Sanders, C. Liao, S. Hagmann, and C. P. Bhalla, Phys. Rev. A **53**, 2272 (1996).
[85] C. O. Reinhold, D. R. Schultz, R. E. Olson, C. Kelbch, R. Koch, and H. Schmidt-Böcking, Phys. Rev. Lett. **66**, 1842 (1991).
[86] E. P. Benis, T. J. M. Zouros, T. W. Gorczyca, M. Zamkov, and P. Richard, J. Phys. B **36**, L341 (2003).
[87] R. H. Landau, *Quantum Mechanics II: A Second Course in Quantum Theory* (John Wiley & Sons, New York, 1990).
[88] P. G. Burke and K. A. Berrington, *Atomic and Molecular Processes: An R-matrix Approach* (Institute of Physics Publishing, Bristol, 1993).
[89] C. H. Froese-Fischer, Comput. Phys. Commun. **64**, 369 (1991).
[90] K. A. Berrington, W. B. Eissner, and P. H. Norrington, Comput. Phys. Commun. **92**, 290 (1995).
[91] K. A. Berrington, P. G. Burke, K. Butler, M. J. Seaton, P. J. Storey, and Y. Yan, J. Phys. B **20**, 6399 (1987).
[92] F. T. Smith, Phys. Rev. **118**, 349 (1960).
[93] F. Robicheaux, T. W. Gorczyca, M. S. Pindzola, and N. R. Badnell, Phys. Rev. A **52**, 1319 (1995).
[94] T. J. M. Zouros, D. Schneider, and N. Stolterfoht, J. Phys. B **21**, L671 (1988).
[95] S. A. Salvini, Comput. Phys. Commun. **27**, 25 (1982).
[96] I. Hoffmann, E. Jager, and U. Muller-Jahreis, Radiat. Eff. **31**, 57 (1976).
[97] N. Stolterfoht, Phys. Rep. **146**, 315 (1987).
[98] A. Itoh, T. Schneider, G. Schiwietz, Z. Roller, H. Platten, G. Nolte, D. Schneider, and N. Stolterfoht, J. Phys. B **16**, 3965

(1983).
[99] A. Itoh, D. Schneider, T. Schneider, T. J. M. Zouros, G. Nolte, G. Schiwietz, W. Zeitz, and N. Stolterfoht, Phys. Rev. A **31**, 684 (1985).
[100] N. Stolterfoht, in *Fundamental Processes in Energetic Atomic Collisions*, edited by H. O. Lutz, J. S. Briggs, and H. Kleinpoppen, Vol. 103 of NATO Advanced Study Institute Series B: Physics (Plenum Publishing Corporation, New York, 1983), pp. 295–318.
[101] D. A. Dahl, J. E. Delmore, and A. D. Appelhans, Rev. Sci. Instrum. **61**, 607 (1990).
[102] D. A. Dahl, SIMION 3D *v6.0* (Idaho National Engineering Laboratory, Idaho Falls, 1996).
[103] U. Fano, Phys. Rev. **124**, 1866 (1961).
[104] W. Fritsch and C. D. Lin, Phys. Rev. Lett. **61**, 690 (1988).
[105] A. Jain, R. Shingal, and T. J. M. Zouros, Phys. Rev. A **43**, 1621 (1991).
[106] T. R. Dillingham, J. Newcomb, J. Hall, P. L. Pepmiller, and P. Richard, Phys. Rev. A **29**, 3029 (1984).
[107] M. Terasawa, T. J. Gray, S. Hagmann, J. Hall, J. Newcomb, P. Pepmiller, and P. Richard, Phys. Rev. A **27**, 2868 (1983).
[108] E. P. Benis, M. Zamkov, P. Richard, and T. J. M. Zouros, Nucl. Instrum. Methods Phys. Res. B **205**, 517 (2003).
[109] P. L. Pepmiller, P. Richard, J. Newcomb, J. Hall, and T. R. Dillingham, Phys. Rev. A **31**, 734 (1985).
[110] M. Clark, D. Brandt, J. K. Swenson, and S. M. Shafroth, Phys. Rev. Lett. **54**, 544 (1985).
[111] J. A. Tanis *et al.*, Nucl. Instrum. Methods Phys. Res. B **10/11**, 128 (1985).
[112] Y. Hahn, Phys. Rev. A **40**, 2950 (1989).
[113] B. F. Davis and K. T. Chung, Phys. Rev. A **39**, 3942 (1989).
[114] P. Richard, in *Atomic Inner-Shell Processes*, edited by B. Crasemann (Academic Press, New York, 1975), Vol. 1, pp. 73–158.
[115] B. Sulik, T. J. M. Zouros, A. Orbán, and L. Gulyás, J. Electron Spectrosc. Relat. Phenom. **114–116**, 191 (2001).
[116] H. I. Hidmi, Ph.D. dissertation, Dept. of Physics, Kansas State University (1993) (unpublished).
[117] T. J. M. Zouros, E. P. Benis, A. González, T. G. Lee, P. Richard, and T. Gorczyca, in *Application of Acceleration in Research and Industry*, 17th International Conference on the Application of Accelerators in Research and Industry, edited by J. L. Duggan, AIP Conf. Proc. No. 680 (AIP, Melville, NY, 2003).